https://doi.org/10.5194/egusphere-2026-7088
Preprint. Discussion started: 23 November 2026
© Author(s) 2026. CC BY 4.0 License.

The Swiss H_2O Hub: water vapor profiles from ground to space

Adrianos Filinis[1,2], Yann Poltera[1,2], Simone Brunamonti[3], Frank G. Wienhold[4], Gonzague Romanens[5], Giovanni Martucci[5], Renaud Matthey[1,5], Alistair Bell[1,2], Alex Weitnauer[3], Steven Brossi[6], Vivienne Artho[4], Anja Brun[4], Thomas Peter[4], Alexander Haefele[5,7], Béla Tuzson[3], Lukas Emmenegger[3], Axel Murk[1,2], and Gunter Stober[1,2]

[1]Institute of Applied Physics, University of Bern, Bern, Switzerland
[2]Oeschger Centre for Climate Change Research, University of Bern, Bern, Switzerland
[3]Laboratory for Air Pollution/Environmental Technology - Empa, Dübendorf, Switzerland
[4]Institute for Atmospheric and Climate Science, ETH Zurich, Zurich, Switzerland
[5]Federal Office of Meteorology and Climatology, MeteoSwiss, Payerne, Switzerland
[6]Mylab elektronik GmbH, Bubikon, Switzerland
[7]Department of Physics and Astronomy, The University of Western Ontario, London, Canada

Correspondence: Adrianos Filinis (adrianos.filinis@unibe.ch), Yann Poltera (yann.poltera@unibe.ch) and Béla Tuzson (bela.tuzson@empa.ch)

Abstract. Water vapor plays a central role in atmospheric radiation, chemistry, and dynamics, yet no single observing technique provides accurate, vertically resolved measurements throughout the atmospheric column. In particular, the upper troposphere and lower stratosphere (UTLS) remain challenging to observe, despite their importance for climate and stratosphere-troposphere exchange. The Swiss H_2O Hub is a collaborative initiative dedicated to improve water-vapor observations from the ground to space through the coordinated deployment of complementary in-situ and remote-sensing techniques. Between 2023 and 2026, coordinated field campaigns comprising 43 balloon launches were conducted from the MeteoSwiss observatory in Payerne, Switzerland. The campaigns combined established reference instruments with newly developed measurement platforms, including the Peltier-cooled frost point hygrometer (PCFH), the high-accuracy balloon-borne laser absorption spectrometer ALBATROSS, and the cryogenically cooled microwave radiometer CRYOWARA. In addition, an alternative cooling approach has been evaluated for the commercial Cryogenic Frost point Hygrometer (CFH) reference instrument, replacing the high-global-warming-potential refrigerant R23 with a dry-ice–alcohol mixture (DIA-CFH). Continuous observations from the Raman lidar RALMO complemented the balloon-borne measurements in the troposphere, while the ground-based microwave radiometer MIAWARA and the satellite-based Microwave Limb Sounder (MLS) provided observations of the middle atmosphere. Below 12 km, intercomparisons show good agreement between the emerging hygrometers and the CFH reference. At 250 m vertical resolution, ALBATROSS and PCFH exhibit mean relative differences in H_2O mixing ratio of $-1.3 \pm 6.1\%$ and $+0.1 \pm 6.4\%$ based on six and nine flights, respectively. Of the corresponding comparison points, 99.2% for ALBATROSS and 99% for PCFH lie within $\pm 20\%$, demonstrating operational-grade performance of both newly developed in-situ instruments. RALMO reproduces tropospheric humidity variability with agreement of $+1.5 \pm 10.2\%$ below 4 km, while larger scatter near the tropopause ($+2.1 \pm 28.6\%$ above 8 km) primarily due to increasing spatial separation between the balloon-borne and ground-based observations. In the UTLS above 12 km, quantitative assessments are made based on a fewer fully validated observations, with ALBATROSS agreeing within $+4.1 \pm 9.9\%$ (4 flights) and PCFH within $+4.6 \pm 7.7\%$ (7 flights) between 12

https://doi.org/10.5194/egusphere-2026-7088
Preprint. Discussion started: 23 November 2026
© Author(s) 2026. CC BY 4.0 License.



and 28 km. In the higher atmosphere, CRYOWARA and MIAWARA agree within $\pm 10\%$ between 30 and 70 km, validating the capability of the new radiometer to continue the long-term water-vapor record. These results demonstrate that the coordinated use of balloon-borne hygrometers, lidar, and microwave radiometry can provide consistent and overlapping observations across the entire atmosphere. This can serve as a framework for future accurate water vapor observations extending from the ground to the mesosphere.

1 Introduction

Water vapor is an essential climate variable of the Earth's atmosphere. It plays a crucial role in the Earth's radiative balance, serving as the most significant greenhouse gas in the upper troposphere (Andrews et al., 1987; Brasseur and Solomon, 2005; World Meteorological Organization (WMO) et al., 2025). It has a positive climate feedback that amplifies warming and roughly doubles the effect of increased CO_2 alone (Andrews et al., 1987; Brasseur and Solomon, 2005). In the lower stratosphere, water vapor continues to have important radiative effects on surface heating and stratospheric temperature structure, and it also influences the formation of polar stratospheric clouds, which in turn modulate heterogeneous chemical reactions and therefore have secondary effects on chemical species such as ozone (Andrews et al., 1987; Brasseur and Solomon, 2005; Steiner et al., 2021). Another ozone-depleting pathway arises because water vapor is a source of HO_x, which participates in catalytic cycles involving atomic oxygen that destroy ozone (Andrews et al., 1987; Brasseur and Solomon, 2005). Further impacts from water in the mesosphere result from radiative cooling, with secondary effects on dynamics, and through noctilucent cloud formation (Andrews et al., 1987; Hervig et al., 2003; Brasseur and Solomon, 2005; Akmaev et al., 2006; Hervig et al., 2015; Gerding et al., 2013). The large number of impacts that changes in water vapor can have makes it an essential variable to monitor accurately throughout the Earth's atmosphere from the surface to space (World Meteorological Organization (WMO) et al., 2025).

Monitoring the atmospheric radiative budget from the troposphere to the upper mesosphere remains a major challenge, especially from the ground (Kandel and Viollier, 2010). A range of in-situ (balloon-, aircraft-, or rocket-borne) and remote sensing (ground-, aircraft-, or space-based) instruments is used to probe the atmosphere, including radiosondes, frost point hygrometers, laser absorption spectrometers, radiometers, radars, and lidars. However, each technique covers a specific altitude range and is characterized by distinct analytical characteristics (Hauchecorne et al., 2009; Barrera-Verdejo et al., 2016).

At present, tropospheric H_2O is routinely measured using radiosondes equipped with polymer-based humidity sensors, such as Vaisala's RS41, widely deployed by the GCOS Reference Upper-Air Network (GRUAN) (e.g. Seidel et al., 2009; Immler et al., 2010; Dirksen et al., 2014; Bodeker et al., 2016). However, operational radiosondes cannot provide lower-stratospheric water-vapor measurements with the accuracy required for climate applications. For the UTLS, GCOS specifies two-sigma uncertainty requirements of 0.1 ppmv (i.e., $\approx 2\%$) in H_2O mixing ratio at 10 m vertical resolution ("goal"), 0.25 ppmv ($\approx 5\%$) at 100 m vertical resolution ("breakthrough"), and 0.5 ppmv ($\approx 10\%$) at 250 m vertical resolution ("threshold"). For the overlying mesosphere, GCOS specifies two-sigma uncertainty requirements of 0.1 ppmv (i.e., $\approx 2\%$) in H_2O mixing ratio at

https://doi.org/10.5194/egusphere-2026-7088
Preprint. Discussion started: 23 November 2026
© Author(s) 2026. CC BY 4.0 License.

0.5 km vertical resolution ("goal"), 0.25 ppmv (≈ 4%) at 1 km vertical resolution ("breakthrough"), and 0.5 ppmv (≈ 8 %) at 3 km vertical resolution ("threshold") (World Meteorological Organization (WMO) et al., 2025).

Cryogenic frost point hygrometry (CFH) is currently regarded as the state-of-the-art balloon-borne method for the UTLS H_2O, with an established uncertainty less than 10% after downsampling and quality flagging (Vömel et al., 2007), and even better under stable operating conditions of the mirror temperature controller (Vömel et al., 2016; Hall et al., 2016) or with newly emerging processing techniques treating for the nonequilibrium error (Poltera et al., 2026). Because the R23 coolant used by CFH must be phased out due to its high global warming potential, alternative technologies are currently being developed, including Peltier cooling (Jorge, 2019) and the use of other cooling agents (e.g., dry ice-alcohol mixtures).

Middle atmospheric H_2O is measured by microwave radiometry, which measures absorption or emission spectra (depending on whether the instrument observes from space or from the ground) (Hartogh and Jarchow, 1995; Nedoluha et al., 1995; Haefele et al., 2009; Mevi et al., 2018; Hallgren and Hartogh, 2012). Global-scale dynamics can be monitored through changes in middle atmospheric water vapor, as illustrated by the observation of the recent underwater volcanic Hunga Tonga–Hunga Ha'apai eruption, which injected within a single day only approximately 146 ± 5 Tg of water vapor into the stratosphere, corresponding to about 10% of the pre-existing global stratospheric water vapor (Millán et al., 2022). In Switzerland, MIAWARA has been retrieving vertical profiles of middle atmospheric H_2O since 2002 (Deuber et al., 2004) and has been consistently validated against the Microwave Limb Sounder (MLS) on board the Aura satellite (Lambert et al., 2007). To ensure the continuation of the measurements, the University of Bern is developing a new-generation water vapor radiometer, called CRYOWARA, to replace MIAWARA (Filinis et al., 2026). CRYOWARA is a cryogenically cooled radiometer with increased sensitivity, which will allow retrieval of atmospheric profiles at higher altitudes and with higher temporal resolution.

The Swiss H_2O Hub project is a collaborative effort involving research teams from the University of Bern, ETH Zurich, Empa (Swiss Federal Laboratories for Materials Science and Technology), and MeteoSwiss, and was launched in December 2022. Its main objective is to improve vertically resolved measurements of atmospheric water vapor from the ground to the mesopause. Particular emphasis is placed on addressing critical observational gaps in the UTLS by building on complementary expertise and instrumentation at the participating institutions, with particular focus on strengthening consistency between measurement techniques, ensuring vertical overlap among observing systems, and advancing the operational readiness of emerging instruments.

This paper presents an overview of all developments that were conducted within the Swiss H_2O Hub framework and provides a summary of the resulting datasets from coordinated measurement campaigns and corresponding intercomparisons that demonstrate the potential of synergistic observations to deliver vertically resolved water-vapor measurements throughout the entire atmosphere. Section 2 provides an overview of each instrument. Section 3 describes the campaign design and flight strategies. Section 4 presents the intercomparison results, structured into three altitude regions: the troposphere, the UTLS, and the extended profile from the ground to the mesopause. Section 5 provides a discussion of the results.

https://doi.org/10.5194/egusphere-2026-7088
Preprint. Discussion started: 23 November 2026
© Author(s) 2026. CC BY 4.0 License.

2 Instruments

The instrument descriptions provided below focus on their development within the framework of the project, including the initial configurations, key technical advancements achieved, and their current performance status. A comprehensive technical description of each instrument is beyond the scope of this paper; detailed information can be found in the referenced literature.
90 An overview of the instrument suite is shown in Table 1, and an illustrative overview of their respective altitude coverages is shown in Figure 1.

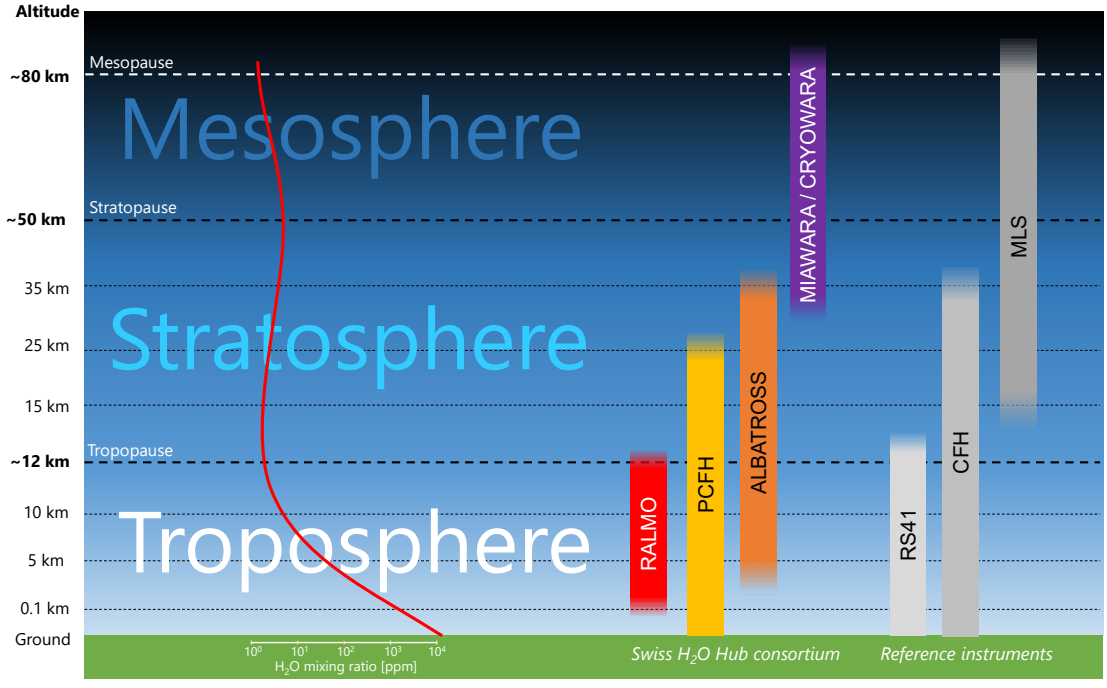

Figure 1. Observational framework of the Swiss H_2O Hub. The altitude ranges of the participating instruments are shown relative to an idealized atmospheric water-vapor profile. The overlapping observations from complementary in-situ, ground-based, and satellite techniques can bridge atmospheric regions that differ by more than four orders of magnitude in water-vapor mixing ratio. The overlap regions enable intercomparison, validation, and transfer of traceability between independent measurement principles, thereby establishing an integrated water-vapor observing system from the lower troposphere to the upper mesosphere.

https://doi.org/10.5194/egusphere-2026-7088
Preprint. Discussion started: 23 November 2026
© Author(s) 2026. CC BY 4.0 License.

Table 1. List and specifications of the instruments involved in the water vapor measurements from ground to space. All indicated precisions refer to the percentage of H_2O mixing ratios.

Instrument	Type / Principle	Platform	Accuracy / Precision / Resolution
MIAWARA (Uni Bern)	Microwave radiometer (passive) at 22 GHz	Ground-based	Profiles with acceptable response from ∼30–70 km; ∼14–19 km vertical resolution; relative agreement with MLS within ∼10% (Bell et al., 2025b)
CRYOWARA (Uni Bern)	Microwave radiometer (passive) at 22 GHz, cryogenic front end	Ground-based	∼30–80 km, ∼12–17 km vertical resolution (under validation); improved sensitivity: ≈7 mK in 2 h 30 min (Filinis et al., 2026)
RALMO (MeteoSwiss)	Raman lidar (nighttime for UTLS) at 354.7 (407.5, 386.7) nm	Ground-based	∼5–10% vs RS41 up to ∼12 km (night); ∼5% up to ∼4–5 km (day)
ALBATROSS (Empa)	Open-path laser absorption spectroscopy at 1662.809 cm^{-1}	Balloon-borne	Accuracy $< \pm 1.5\%$, precision < 30 ppb ($\sim 0.3\%$) at 1 s resolution in range 2.5–35 ppm, 30–250 hPa (Brunamonti et al., 2023) (laboratory-based validation)
PCFH (mylab, ETH/Uni Bern)	Chilled-mirror hygrometer, electric cooling	Balloon-borne	PCFH/CFH slope 1.008 ± 0.008; accuracy ∼11%; ∼50 m in the UTLS (4-600 ppmv) (Wienhold et al., 2022); mean deviation to CFH 1.7% ± 7.2%; 0-28 km; ∼250 m (this work)
CFH (EN-SCI)	Chilled-mirror hygrometer, cryogenic cooling (R23)	Balloon-borne	Typically < 0.5 K in frost point (∼10%); best < 0.2 K (∼4%); ∼125 m (Vömel et al., 2007; Vömel et al., 2016)
DIA-CFH (EN-SCI, ETH/Uni Bern)	Chilled-mirror hygrometer, dry-ice/ethanol cooling (R23 replacement)	Balloon-borne	Mean deviation -0.3% ± 4.5% vs R23-CFH; 0-28 km; ∼250 m (this work)
RS41 (Vaisala Oy)	Polymer-based capacitive humidity sensor	Balloon-borne	4 %RH at air temperature > −60°C (Vaisala, 2024)
MLS/Aura (NASA)	Microwave limb sounder (passive), 190 GHz radiometer	Satellite (limb-viewing)	4–9%, ∼3 km vertical resolution (UTLS); global coverage (Lambert et al., 2007); limited overpass 6 days per month above Switzerland since May 2024

https://doi.org/10.5194/egusphere-2026-7088
Preprint. Discussion started: 23 November 2026
© Author(s) 2026. CC BY 4.0 License.

2.1 Ground-based instruments

2.1.1 MIAWARA: MIddle Atmosphere WAter vapor RAdiometer

The passive remote sensing radiometer MIAWARA has been operated since 2002 by the University of Bern (Deuber et al., 2004). The instrument measures the rotational transition emission line of water vapor at 22 GHz. Due to the low tropospheric opacity at this frequency, ground-based instruments are suitable for observations even from sea level (Janssen, 1993; Ulaby et al., 2013). The radiometer has been installed at the Zimmerwald observatory (46.945° N/ 7.545° E and 950 m altitude) since 2006 (Bell and Murk, 2023). The instrument relies on a rotating flat reflector that is oriented at different viewing angles depending on the measurement type: line measurements, calibration, and tropospheric opacity calculation. To remove unwanted reflections between the receiver and the different targets (standing waves), the flat mirror is mounted on a linear translation stage, which changes the distance between the horn antenna and reflector by a quarter wavelength. This way, the phase of the standing waves changes and, by averaging between the two positions, the errors induced by standing waves are minimized (Gustincic, 1977). MIAWARA is currently able to provide retrievals of water vapor profiles from 30 km to 70 km with an acceptable measurement response (MR > 0.8) (Schranz et al., 2019).

2.1.2 CRYOWARA

CRYOWARA is a new radiometer under development by the University of Bern as part of the Swiss H_2O Hub project. It represents the long-term remote-sensing component of the Swiss H_2O Hub. In contrast to the in-situ systems, whose primary goal is to improve the quality of campaign-based measurements in the troposphere and UTLS, CRYOWARA will ensure the continuity of ground-based microwave observations of middle-atmospheric water vapor. It will replace MIAWARA at the Zimmerwald observatory in the near future. CRYOWARA is designed with a cryogenic front end, reducing the receiver noise temperature and increasing the sensitivity. All the technical details of CRYOWARA are explained in Filinis et al. (2026). Figure 2a shows the model presentation of the final instrument.

Over the course of the project, the development of CRYOWARA progressed from laboratory-based breadboard work to a prototype (see Figure 2a), before reaching its final configuration for routine operations (see Figure 2c). In particular, after the instrument was partly integrated in its final frame and installed on the roof of the university building, it underwent tests during several months, such as calibration applying different techniques (liquid nitrogen, tipping curve, frequency switch) as well as sun scan measurements to characterize the antenna pattern of the instrument and to validate the alignment of the optics.

After validation of the instrument, and once permanently installed at the Zimmerwald observatory, CRYOWARA is expected to provide a substantial improvement in sensitivity compared to MIAWARA and to strengthen the long-term capability of the Swiss H2O Hub to connect campaign-based observations with continuous ground-based monitoring.

An important distinction between the CRYOWARA and MIAWARA is their radiometric resolution, ΔT_{rms}. The two instruments differ in two respects that both enhance the sensitivity of CRYOWARA: its cryogenically cooled front end lowers the receiver noise temperature T_{rec}, and its dual-polarization receiver further reduces the noise by a factor of $\sqrt{2}$ through polarization averaging (Filinis et al., 2026). As a result, MIAWARA requires 24 hours of integration to reach a radiometric resolution

https://doi.org/10.5194/egusphere-2026-7088
Preprint. Discussion started: 23 November 2026
© Author(s) 2026. CC BY 4.0 License.

of ≈ 6.6 mK at a channel bandwidth of $B \approx 12.2$ kHz, whereas CRYOWARA attains the same value eight times faster. This higher sensitivity is particularly valuable at higher altitudes, where the amplitude of the water-vapor emission line becomes weaker and more difficult to detect (Hallgren et al., 2010).

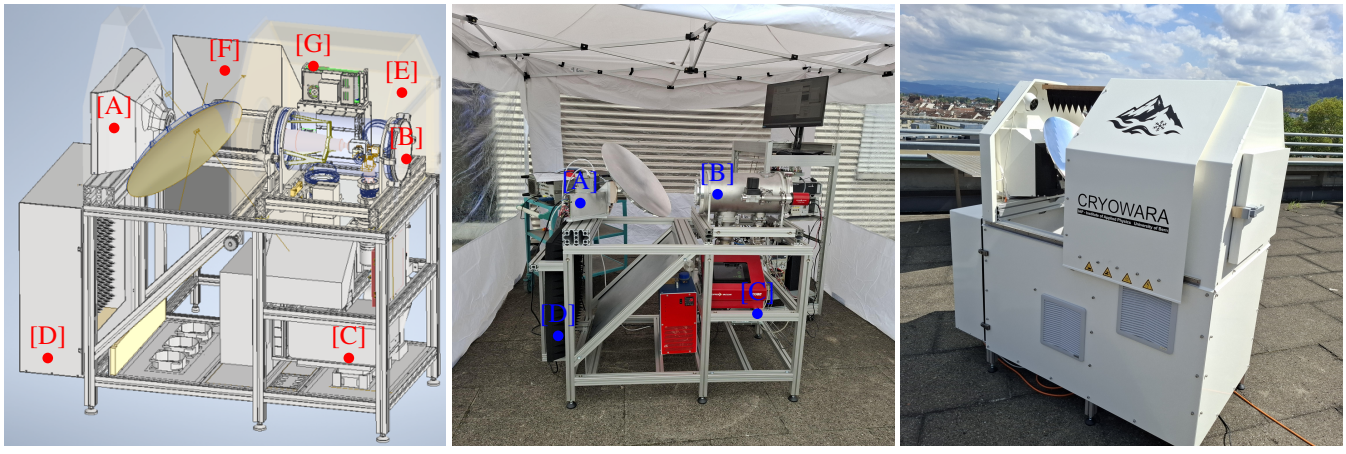

(a) (b) (c)

Figure 2. The CRYOWARA instrument. **(a)** Model representation in its final configuration. **(b)** Instrument deployed (second breadboard phase) on the roof of the University of Bern for its outdoor validation. **(c)** Photograph of the newly developed instrument, installed on the roof of UniBe for final testing and validation. Components marked in (a) and (b): [A] housing of the mirror drive mechanism, [B] vacuum chamber, [C] vital components for the operation of the instrument, e.g., vacuum pump, cryocooler, computer, etc., [D] calibration load with flat reflector, [E] rain-hood, [F] occasional LN2 calibration target, [G] front end and power supplies.

2.1.3 RALMO

RAman Lidar for Meteorological Observations (RALMO) is an operational Raman lidar system located at the MeteoSwiss site in Payerne and has been providing continuous atmospheric profiling since 2008 (Dinoev et al., 2013). The system routinely retrieves atmospheric water vapor mixing ratio, temperature, and aerosol properties with high vertical and temporal resolution.

A particular strength of RALMO is its ability to provide near-continuous humidity profiling, complementing the twice-daily radiosonde observations typically available from operational upper-air networks. Depending on atmospheric conditions and background illumination, water-vapor profiles are available with approximately half-hourly temporal resolution and typically extend through much of the troposphere, reaching the tropopause during nighttime in clear sky conditions.

The high data availability enables the investigation of fast atmospheric processes (e.g., Figure 3) and long-term variability. The RALMO data span almost two decades and represents therefore a unique climatological dataset for the study of tropospheric humidity trends (Hicks-Jalali et al., 2020; Chouza et al., 2022; Jayaweera et al., 2025), assimilation into numerical weather prediction (Leuenberger et al., 2020; Crezee et al., 2025), and aerosol and temperature studies (Navas-Guzmán et al., 2019; Díaz-Zurita et al., 2026; Brunamonti et al., 2021; Masoom et al., 2026; Sica and Haefele, 2015; Martucci et al., 2021;

https://doi.org/10.5194/egusphere-2026-7088
Preprint. Discussion started: 23 November 2026
© Author(s) 2026. CC BY 4.0 License.

Farhani et al., 2023) over central Europe. Such long-term measurements are essential for improving the understanding of atmospheric moistening, boundary-layer processes, and transport phenomena extending into the lower stratosphere.

Within the Swiss H_2O Hub, RALMO represents the continuous tropospheric component of the observing system. Its measurements provide the temporal context for the balloon campaigns and enable direct comparison with in-situ observations from CFH, PCFH, and ALBATROSS. The long-term record furthermore links campaign-based observations to climate-monitoring applications and international observing networks including ACTRIS, NDACC, and GRUAN.

Figure 3 illustrates a representative 10-day period of water vapor mixing ratio measured by RALMO, highlighting the substantially higher temporal sampling achieved by RALMO compared with routine radiosonde observations (shown as vertical dashed lines in the figure). RALMO delivers near-continuous humidity profiling with half-hourly resolution under favorable atmospheric conditions, enabling the observation of rapidly evolving moisture structures. By continuously monitoring the thermodynamic state of the atmosphere, RALMO provides valuable information to numerical weather models and forecasters to improve weather predictions.

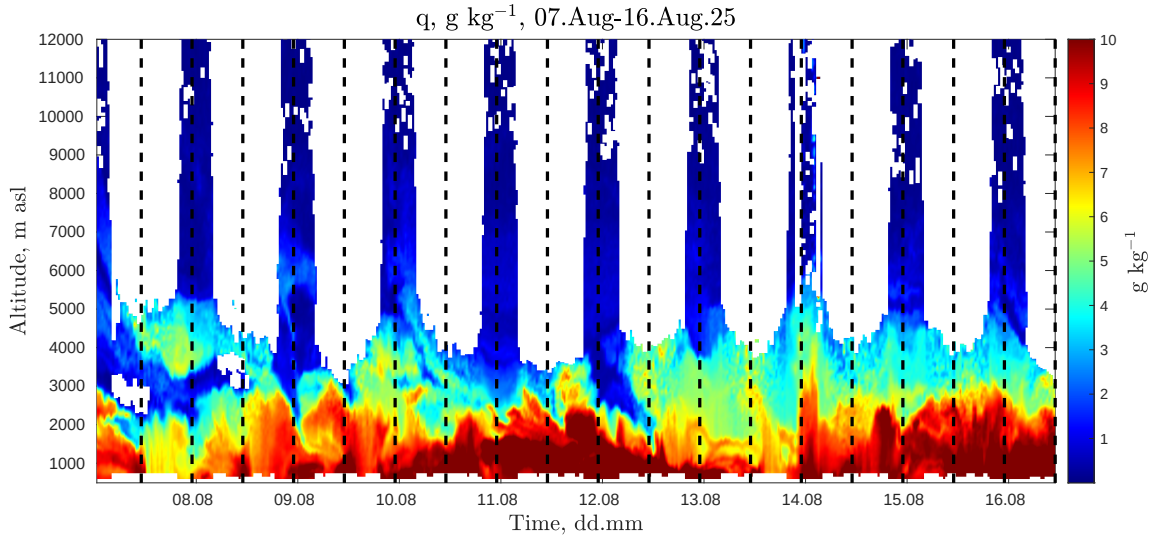

Figure 3. Time series of RALMO's water vapor mass mixing ratio during ten consecutive days from 7 to 16 August 2025. The vertical dashed lines show the time of a radiosonde sounding at 11 UT and 23 UT. The white areas correspond to data that have been filtered out due to low signal-to-noise ratio.

2.2 In-situ instruments

2.2.1 ALBATROSS

The balloon-borne laser absorption spectrometer for UTLS water research, ALBATROSS, is a compact, open-path, quantum-cascade laser absorption spectrometer designed for balloon-borne measurements of water vapor in the UTLS (Graf et al., 2021). Its development responds to the need for highly accurate, SI-traceable H_2O measurements at vertical resolutions of a

https://doi.org/10.5194/egusphere-2026-7088
Preprint. Discussion started: 23 November 2026
© Author(s) 2026. CC BY 4.0 License.

few meters. The spectrometer uses direct absorption spectroscopy in the mid-infrared, targeting a strong and spectroscopically well-characterized H_2O absorption line at 1662.809 cm^{-1}. A custom-developed segmented circular multipass cell with 10.8 cm diameter provides an optical path length of 6.1 m (Graf et al., 2018). The full instrumental payload weighs 3.6 kg, making it compatible with standard meteorological balloons.

A series of laboratory-based validation activities (Brunamonti et al., 2023, 2025) assessed the spectrometer's performance at UTLS-relevant conditions and established its traceability to the SI. These studies demonstrated an accuracy better than ± 1.5 % down to 2.5 ppm H_2O against SI-traceable reference gases generated by a dynamic-gravimetric permeation method, and a precision better than 30 ppb at 1 s resolution (Brunamonti et al., 2023). The performance of the spectrometer was further evaluated within the AquaVIT-4 intercomparison of atmospheric hygrometers across a dynamic range of $0.5 - 530$ ppm H_2O and a wide range of challenging environmental conditions (Brunamonti et al., 2025).

ALBATROSS was deployed in six balloon flights of the Swiss H_2O-Hub project, which are discussed in detail in Brunamonti et al. (2026). Throughout these flights, the instrument underwent iterative hardware modifications in response to the findings of each flight. In particular, technical challenges related to contamination from internal moisture within the instrument's enclosure emerged in early flights and required targeted design improvements. This included, most notably, the development of an in-flight purging system, aiming to suppress absorption contributions from outside the multipass cell, and a redesign of the intake tube system. A detailed overview of these technical challenges and a flight-by-flight description of the instrument's configuration and performance can be found in Brunamonti et al. (2026).

2.2.2 PCFH: Peltier-cooled frost point hygrometer

The Peltier-Cooled Frost Point Hygrometer (PCFH) (Wienhold et al., 2024) has been developed as an alternative to the cryogenic frost point instruments NOAA FPH (Mastenbrook and Oltmans, 1983) and CFH (Vömel et al., 2007), which rely on the refrigerant R23 being phased out. The instrument is designed as a dual-channel system comprising two sub-units sharing common electronics, controller, and housing. Frost point temperatures are achieved using two-stage Peltier elements, with heat dissipation facilitated by ambient airflow. The PCFH uses polished, gold-plated copper mirrors tilted out of specular reflection to enable detection of light scattered by the condensate. A modulated LED illuminates both the mirror and a reference surface, and the resulting signals are imaged onto two silicon photodetectors and extracted by phase-sensitive detection (Figure 5). The frost point is determined by maintaining a constant optical signal corresponding to a stable ice layer. The instrument provides measurements at a temporal resolution of 1 s, corresponding to a vertical resolution of approximately 5 m under typical balloon ascent rates. The current design (42×30×15 cm^3, 1.5 kg including batteries) is suitable for routine balloon-borne operation. The cooling capacity and signal-to-background ratio enable reliable measurements up to ∼20 km during daytime and at least 25 km during nighttime conditions at mid-latitudes.

During the project, the PCFH has undergone several design revisions, targeting cooling efficiency, optical signal quality, and temperature measurement and control. Thermal management of the Peltier hot side was enhanced through the development of a lightweight, modular heat sink based on stacked aluminum elements, improving cooling performance by approximately 15 K. This extended the operational altitude range from ∼15 km to at least 25 km for nighttime soundings.

https://doi.org/10.5194/egusphere-2026-7088
Preprint. Discussion started: 23 November 2026
© Author(s) 2026. CC BY 4.0 License.

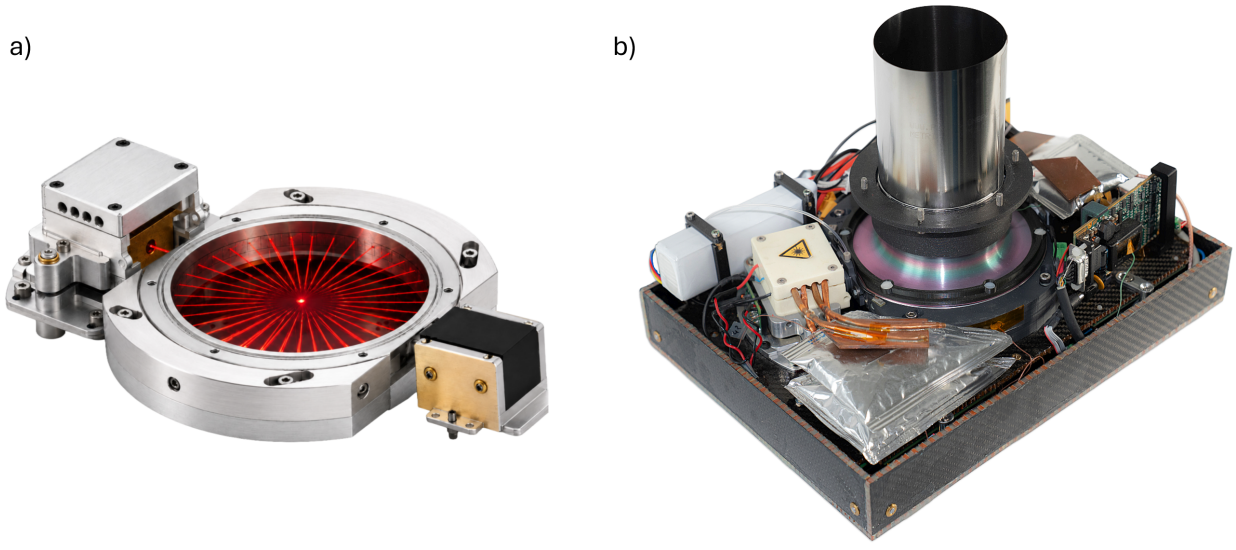

Figure 4. ALBATROSS open-path laser hygrometer for UTLS water-vapor observations. (a) Optical layout comprising a quantum cascade laser, segmented circular multipass cell (SC-MPC), and IR detector. The long effective absorption path provided by the SC-MPC enables sensitive spectroscopic measurements down to a few ppm. (b) Flight configuration (thermal insulation and top cover removed) deployed during the Swiss H_2O Hub validation campaigns (Brunamonti et al. (2026)). ALBATROSS combines compact size, low mass, rapid response time, and SI-traceable laser spectroscopy, providing an alternative measurement principle to chilled-mirror hygrometers for balloon-borne water-vapor observations.

The optical system was redesigned to increase signal contrast and measurement sensitivity. Using a commercial objective lens increased the contrast between clean and iced mirror states by about 3-fold. A revised control strategy was implemented, using a fixed fraction of the optical contrast as the feedback setpoint, ensuring reproducible ice layer conditions and improved responsiveness of the frost point tracking. The Arrhenius-law frost point characteristic is compensated in the temperature dependence of the controller gain, yielding a tighter frost point tracking while avoiding controller instability.

Temperature measurements of mirrors, air, reference surfaces, and internal diagnostics are performed using T-type thermocouples referenced to the national standard of the Swiss Federal Institute of Metrology (METAS). Early configurations exhibited temperature biases (0.5 K) due to internal gradients within the thermocouple module (TCM). An offset in mirror temperature quantified as 80% ($\pm$ 20%) of the junction's internal temperature difference had to be accounted for. These effects were mitigated by thermal decoupling of the TCM, improved junction design, and additional diagnostic measurements enabling internal corrections. The time constant of the reference temperature measurement was quantified as 31 s ($\pm$ 5 s). As a result, the temperature accuracy compared to the Vaisala RS41 radiosonde air temperature improved to $\pm$100 mK (Wienhold et al., 2025), consistent with radiosonde specifications and leading to an agreement with the CFH below the $\approx$ 20% breakthrough level defined by CIMO (WMO, 2024:Annex 12.A) for the lower stratosphere (Poltera et al., 2026).

https://doi.org/10.5194/egusphere-2026-7088
Preprint. Discussion started: 23 November 2026
© Author(s) 2026. CC BY 4.0 License.

The electronic system was redesigned, and the signal acquisition migrated from an FPGA-chip to a microcontroller-based architecture. Exploiting the high data throughput of the embedded analog peripherals yielded increased sampling rates and reduced noise levels in simplified electronics. The core operation of the PCFH electronics has been proven during the flights carried out in 2026, followed by controller fine-tuning and the phasing-in of new features, such as proprietary pressure and global navigation satellite system (GNSS) sensors. The internal power distribution and the Peltier drivers were revised, reducing mass and simplifying the battery pack arrangement. These modifications were accompanied by the redesign and modularization of the mechanical/thermal modules. The changes were continuously verified in flights used for validation.

Additional features include integrated pressure sensing for autonomous reaction to external conditions, countermeasures against contamination by heating the optical units more strongly, and by adding output stages for future inlet tube heating (Jorge et al., 2021). A new interface is foreseen for a GNSS receiver and an optional inertial measurement unit with a compass. These developments consolidated the fabrication know-how elaborated jointly between ETH and mylab elektronik GmbH. The aim is to commercialize the instrument and ensure its long-term availability.

An early PCFH prototype was previously evaluated during comparison flights performed in tandem with the CFH reference instrument. Up to the lower stratosphere, the measurements showed good agreement, with a regression slope of 1.008 ± 0.008 (Wienhold et al., 2022). This is statistically indistinguishable from unity and demonstrates that Peltier-based cooling can reproduce cryogenic frost point measurements without introducing detectable systematic scaling biases throughout the sampled atmospheric column.

https://doi.org/10.5194/egusphere-2026-7088
Preprint. Discussion started: 23 November 2026
© Author(s) 2026. CC BY 4.0 License.

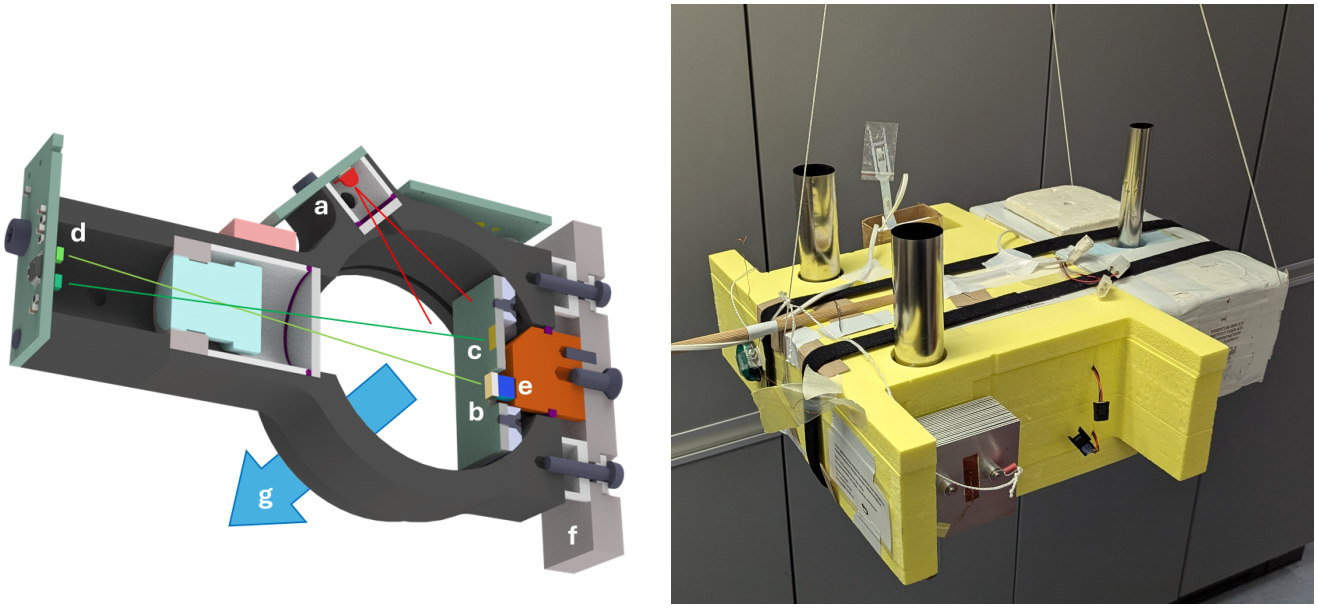

Figure 5. Schematics of a PCFH sub-unit (left). An LED (a) illuminates the plane with a mirror (b) and a reference surface (c) that are imaged on two detectors (d). The mirror is mounted on a Peltier element (e), which is attached to a heat-sink adapter (f) permitting cooling by adaptable heat sink devices exposed to the ambient air flow as well as the interior of the assembly with air streaming from top to bottom during balloon ascent (g). Right: ready-to-fly balloon payload including PCFH, CFH, and iMet-4 (on the back). The RS41 is mounted on a stick to the left, not visible in the picture.

2.2.3 CFH

The Cryogenic Frost Point Hygrometer (CFH) (EN-SCI) is a state-of-the-art balloon-borne instrument for measuring water vapor from the ground up to $\sim$ 28 km altitude (Vömel et al., 2007; Vömel et al., 2016; Hall et al., 2016). It is designated as a reference instrument by the WMO (Nash et al., 2011; Dirksen et al., 2024) and serves as the primary reference instrument for the Swiss H_2O Hub. The CFH is based on the cryogenic chilled mirror technique and measures the frost point of air with an SI-traceable uncertainty less than 0.5 K (or 10% in H_2O mixing ratio) at 125 m vertical resolution under most conditions (Vömel et al., 2007). Under optimized conditions such as stable frost control (Fahey et al., 2014; Vömel et al., 2016) or at so-called Golden Points (Poltera et al., 2021, 2026), the uncertainty may be less than 0.2 K (or 4% in H_2O mixing ratio (Hall et al., 2016)).

Within the Swiss H_2O Hub campaigns, CFH instruments were deployed in all 32 flights, in combination with RS41 radiosondes using MW41 telemetry (Vaisala, 2021, 2024). These measurements provided a consistent reference for intercomparison and validation of the other observing systems.

CFH uses R23 (CHF_3 or fluoroform) as a cryogen. Owing to its high global warming potential (GWP) of 14,800 (UNEP, 2016), this substance is being phased out. The estimated emissions are about 7 equivalent tons of CO_2 per balloon sounding with a CFH payload. Within the Swiss H_2O Hub, efforts have therefore focused on evaluating alternative cooling, such as

https://doi.org/10.5194/egusphere-2026-7088
Preprint. Discussion started: 23 November 2026
© Author(s) 2026. CC BY 4.0 License.

dry ice and alcohol (DIA), and advancing Peltier-based instruments, with the intention to reduce environmental impact while maintaining measurement performance of chilled mirror hygrometry.

2.2.4 DIA-CFH

As a low GWP alternative to the standard CFH configuration, a dry ice-alcohol (DIA) cooling mixture was used in approximately half of the balloon payloads. In this configuration, the CFH instrument (with standard firmware version 6.44) is operated with a cryogen consisting of solid CO_2 (dry ice) and ethanol, replacing the conventional refrigerant R23. The DIA-CFH retains the same size, geometry, inlet system, electronics, and mirror temperature calibration as the standard CFH ($12 \times 17 \times 31$ cm^3, ~900 g including coolant), as well as identical inlet tubing (17 cm length, 2.5 cm diameter). This approach had already shown potential for reliable sounding (Dirksen, 2020; Rolf et al., 2020).

Initial tests within the Swiss H_2O Hub were based on the setup described by Rolf et al. (2020), in which dry ice pellets (16 mm diameter) were immersed in ethanol. Two incremental follow-up improvements were introduced: i) the addition of a thin aluminum plate in thermal contact with the cold finger, aimed at improving the thermal inertia of the cold bath, and ii) the preparation method of a homogeneous cold mixture, by grinding the dry ice pellets before mixing, followed by intensive stirring, thereby improving thermal contact with the cold finger and maintaining a highly viscous mixture during parachuted descent.

Due to the higher sublimation temperature of CO_2 compared to the boiling point of R23, the cooling capacity of DIA is lower. Nevertheless, the achievable minimum temperature, constrained by the ethanol freezing point (around -114°C), is sufficient to cover both tropospheric and stratospheric frost point requirements. A limitation of the DIA-CFH approach is the increased risk of losing frost control during large frost point depressions, especially during the second cleaning cycle at -53°C. In these situations, the cold mixture typically reaches around -80°C compared to -95°C for R23, resulting in a recovery time that is about three times longer ($\sim$ 135 s or $\sim$ 0.7 km). If the cleaning cycle occurs in the stratosphere, this delay can be significantly longer and thus degrade or invalidate parts of the stratospheric profile.

The measurement protocol follows that of the standard CFH, with two cleaning cycles applied during ascent: the first at -15°C dew point, ensuring mirror condensate transition from (supercooled) dew to hexagonal ice (I_h), and the second at -53°C frost point, to establish a thin and responsive ice layer I_h condensate for stratospheric measurements. The first kilometers of parachuted descent are generally not used, due to suboptimal payload orientation and flow conditions relative to the inlet geometry (optimized for $\sim$ 5 m/s ascent and near-zenith pointing, i.e. $\lesssim 25°$ tilt angle (Jorge et al., 2021)). In addition, the same limitations related to contamination apply as for the standard CFH, including hydrometeor interference in the troposphere and balloon outgassing in the stratosphere, restricting the maximal retrieval altitude to about 28 km under clear sky conditions (Vömel et al., 2007; Jorge et al., 2021).

2.3 Auxiliary Measurements

Besides the primary in-situ and remote sensing instruments, a set of auxiliary measurements was used during the Swiss H_2O Hub campaigns to provide additional thermodynamic, dynamical, and large-scale atmospheric information. The Vaisala RS41

https://doi.org/10.5194/egusphere-2026-7088
Preprint. Discussion started: 23 November 2026
© Author(s) 2026. CC BY 4.0 License.

(all payloads) and InterMet iMet-4 (additionally to RS41 on PCFH payloads) delivered profiles of pressure, temperature, humidity, position, and wind, while a 9-axis inertial measurement unit (IMU, WitMotion WT901SDCL) was used to characterize the motion and orientation of the balloon payload during some of the flights.

2.3.1 RS41

Vaisala RS41 sondes were used to provide high-vertical-resolution profiles of pressure, temperature, relative humidity, position, and wind. The RS41 is a widely used operational radiosonde equipped with a heated thin-film capacitive humidity sensor, a temperature sensor, and GPS-based positioning (Jensen et al., 2016; Sun et al., 2021). Compared with the previous RS92 generation, the RS41 shows improved humidity performance and reduced uncertainty, which has contributed to its widespread adoption in operational and reference upper-air networks (Jensen et al., 2016; Dirksen, 2020). The manufacturer-specified resolution and combined uncertainty of humidity measurements by RS41 are 0.1% RH and 4% RH, respectively, at ambient air temperature $> -60°C$ (Vaisala, 2024).

2.3.2 Satellite measurements from MLS

In addition to the in-situ and ground-based observations, satellite measurements were used to place the campaign results into a broader spatial and temporal context. For this purpose, data from the Microwave Limb Sounder (MLS) onboard NASA's Aura satellite were used as well. MLS is a passive microwave limb sounder that measures thermal emission from the atmospheric limb and retrieves vertical profiles of trace gases, temperature, pressure, and cloud-related variables (Waters et al., 2006; Jet Propulsion Laboratory, 2020). For water-vapor studies, one of the main advantages of this technique is its near-global day-and-night coverage and ability to provide measurements under conditions that are challenging for shorter-wavelength techniques, such as the presence of ice clouds or aerosols (Waters et al., 2006; NASA, 2025). For the standard H_2O product, the recommended useful vertical range extends from about 316 to 0.00215 hPa, with a vertical resolution of roughly 1.5 to 3.5 km depending on altitude (NASA GES DISC, 2020; Jet Propulsion Laboratory, 2020). As Aura MLS approaches the end of its operational lifetime, its 190- GHz water-vapor observations have been duty-cycled to roughly six days per month since May 2024 to conserve instrument life (and no further scheduling is foreseen since Fall 2026) (MLS Science Team, 2024, 2026; NASA, 2026b, a). As a result, coincident observations over Switzerland have become increasingly sparse.

3 Campaign description

All balloon flights were conducted from the MeteoSwiss station in Payerne (46.813° N, 6.943° E, 490 m asl, WMO 06610), which is part of the global network of reference stations for climate monitoring (GRUAN-GCOS Reference Upper-Air Network), the Aerosol, Clouds and Trace Gases Research Infrastructure (ACTRIS), and the network for the detection of atmospheric composition change (NDACC). A total of 32 flights were completed, and all balloon-borne payloads were recovered after each flight. Instrument recovery was a primary consideration in mission planning, and a recovery rate of 100% represents a key operational outcome. An overview of all flights is provided in Table A1.

https://doi.org/10.5194/egusphere-2026-7088
Preprint. Discussion started: 23 November 2026
© Author(s) 2026. CC BY 4.0 License.

In Switzerland, payloads exceeding 2 kg require specific authorization from the Swiss Federal Office of Civil Aviation (FOCA). This authorization provides the regulatory framework for coordinating flights and applicable airspace restrictions with the Swiss air navigation service provider (Skyguide), in accordance with the classification defined in EC (2012). According to this framework, payloads weighing up to 3 kg (e.g., PCFH/CFH and CFH/CFH intercomparison flights) fall within the "lightweight" classification and are subject to relatively low restrictive operational requirements. In contrast, payloads exceeding 3 kg, including ALBATROSS and ALBATROSS/CFH configurations, are classified as "heavy" and are subject to additional operational constraints. These constraints included (*i*) nighttime operation (22:00–06:00 LT), (*ii*) installation of a transponder, aviation lights, and redundant flight termination devices, (*iii*) specific coordination with Skyguide, and (*iv*) confinement of the flight trajectory within Swiss airspace. To comply with these requirements, ALBATROSS payloads were equipped with a lightweight transponder (Ping20Si, uAvionix, USA), aviation lights, and redundant flight termination devices, including a cut-down system (HAB Bounder, Loonatec, USA). The cut-down system provided a geofencing capability by automatically terminating the flight when a predefined altitude ceiling was reached, thereby helping to constrain the balloon trajectory within the authorized airspace. An independent redundant termination device provided an additional means of terminating the flight in the event of failure of the primary cut-down system.

For accurate water vapor measurements in the UTLS, particular attention was given to minimizing contamination from tropospheric moisture. Desorption/evaporation/sublimation of H_2O molecules from the balloon train or payload can lead to significant biases in dry upper-atmospheric conditions. In particular, mixed-phase clouds are a well-known source of contamination in CFH measurements, as supercooled water droplets can freeze within the inlet of the instrument and subsequently sublimate at higher altitudes (Jorge et al., 2021). Therefore, launches were scheduled under dry conditions in the middle troposphere (altitude range $\sim 4-10$ km), avoiding precipitation and near-saturated mix-phase environments based on weather forecasts. Before launch, the weather conditions were monitored using the instruments at Payerne and all available meteorological forecasts.

Low-level liquid clouds, fog, and fully glaciated cirrus clouds (below the homogeneous freezing temperature, $-38°C$) were considered acceptable for the balloon launches, although they may reduce lidar visibility. To further mitigate contamination from the balloon surface, all payloads were equipped with a 60 m unwinder (GRAW, Germany), increasing the separation between the balloon and the instrument payload.

To ensure reliable payload recovery after each flight, launch opportunities were additionally constrained by the forecasted balloon trajectory, i.e., the atmospheric wind field. Particularly, flights were excluded if predicted landing locations were in areas where recovery could not be guaranteed, such as regions near lakes or complex mountainous terrain (high alpine landing sites above 2000 m). For payloads equipped with a Mode-S transponder (Droniq GmbH, 2024), crossings of international borders had to be avoided; therefore, geofencing constraints were additionally applied. This requirement was particularly restrictive for ALBATROSS flights, as the instrument is a unique prototype.

Trajectory forecasts were performed using multiple tools and models to ensure robustness, including LAGRANTO driven by IFS forecast data (Sprenger and Wernli, 2015), and the NOAA GML balloon-trajectory-prediction model based on GFS forecast data (NOAA Global Monitoring Division, 2026). Moreover, Sondehub tools (SondeHub, 2026) were an added value

https://doi.org/10.5194/egusphere-2026-7088
Preprint. Discussion started: 23 November 2026
© Author(s) 2026. CC BY 4.0 License.

for both planning and recovery. Through this multi-model approach and conservative selection criteria, all payloads launched within the Swiss H_2O Hub project were successfully recovered.

To further support campaign planning, a statistical analysis of balloon trajectories from operational balloon soundings at Payerne was performed for the period $2019 - 2022$. These soundings, conducted twice daily at 00 and 12 UTC, provide estimated landing locations derived from the last GPS signal measured by the radiosonde. Figure 6 shows the distribution of all landing points, color-coded with time of the year, overlaid with the trajectories of the Swiss H_2O Hub flights. The results highlight the strong seasonality of the balloon trajectories, with landing points located mainly in the Swiss plateau during the summer period, and a systematic shift towards East and the Alpine region in winter due to the mid-latitude jet stream. Consequently, most balloon flights were conducted during the spring and summer seasons.

Flight decisions were based on iterative trajectory forecasts using the most recent meteorological data, including wind speed and direction up to about 35 km. Multiple potential launch windows were evaluated, and the final decision to proceed was based on repeated reassessment of all operational requirements and criteria. This process was typically conducted both on the day preceding a potential nighttime launch and again in the hours immediately before release. During the final launch preparation phase, particular attention was given to updated trajectory predictions and contamination risk, while a standardized launch protocol was adopted to ensure consistent operations.

These preparation procedures have important implications for the interpretation of the dataset. The measurements presented in this work do not originate from arbitrary launch opportunities, but are from flights that satisfied a demanding combination of meteorological, operational, and scientific criteria. Flight preparation and case selection were integral to the experimental design, aiming at maximizing data quality through trajectory forecasting, contamination assessment, and strict launch criteria. Consequently, the generally good agreement observed in the selected case studies reflects instrument performance under conditions deliberately chosen to minimize contamination.

https://doi.org/10.5194/egusphere-2026-7088
Preprint. Discussion started: 23 November 2026
© Author(s) 2026. CC BY 4.0 License.

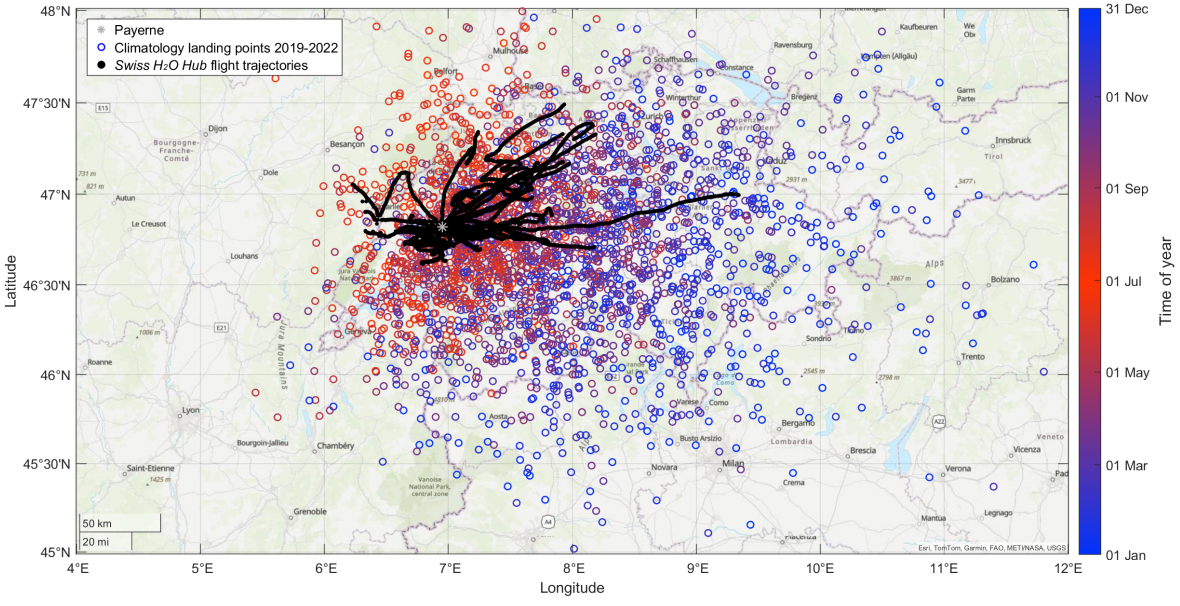

Figure 6. Distribution of landing points of all operational radiosoundings made in Payerne during the years 2019 – 2022 (open circles), color-coded with time of the year, overlaid with individual trajectories of all Swiss H_2O Hub flights (black lines) (map sources: Esri, TomTom, Garmin, FAO, METI/NASA, USGS | Powered by Esri).

4 Results

During the period 2023 – 2026, the participating instruments underwent continuous development, optimization, and validation. As a result, the individual flights listed in Table A1 differ with respect to payload configuration and instrument maturity, and not all flights are equally suited to address the scientific objectives of this work. In the following, we present selected cases that are representative of specific instrument configurations and that best illustrate the performance, complementarity, and limitations of the in-situ and remote sensing instruments, as well as a statistical comparison of all the obtained valid data.

The following sections evaluate the coordinated observations across the different atmospheric regimes targeted by the Swiss H_2O Hub. Particular emphasis is placed on assessing observational consistency between established reference measurements and newly developed instruments, the complementarity of in-situ and remote sensing techniques, and the extent to which the combined observing system can provide continuous water-vapor information from the troposphere to the middle atmosphere. The discussion progresses from individual instrument intercomparisons to an assessment of the integrated observing framework and its implications for future climate-quality water-vapor observations. Its instrument data collection has to be evaluated separately before it is used for analysis. The following paragraphs introduce the data processing followed for the in-situ instruments and RALMO, which are compared from 0-35 km.

https://doi.org/10.5194/egusphere-2026-7088
Preprint. Discussion started: 23 November 2026
© Author(s) 2026. CC BY 4.0 License.

ALBATROSS. The spectral retrieval typically starts at 2–4 km altitude, as the selected spectral window becomes saturated at high H_2O mixing ratios close to the surface (Graf et al., 2021). For intervals affected by contamination from internal moisture within the instrument's enclosure as well as external moisture sources (strings, balloon, sublimation of hydrometeors), common to all balloon-borne hygrometers (e.g., Vömel et al. (2007); Brunamonti et al. (2018); Jorge et al. (2021)), the data were filtered, as described in detail in Brunamonti et al. (2026).

CFH. Data have been quality-checked following standard procedures for balloon-borne frost point hygrometry. This consists of the removal of cleaning-cycle data twice per sounding ascent, at -15 and -53°C frost point temperature for the CFH, cases of operational failure such as PID misbehavior leading to large non-equilibrium or blank-mirror errors, and intermittent contamination during ascent in the stratosphere from moist plumes originating from the outgassing balloon skin, which depends on atmospheric conditions, time of day, and payload motion, or from inlet tubes that may have frozen within supercooled clouds encountered in the troposphere (e.g. Vömel et al. (2007); Vömel et al. (2016); Hall et al. (2016); Brunamonti et al. (2018); Jorge et al. (2021); Poltera et al. (2026)). The Golden Points analysis is used as additional quality control of the data processing. It provides a new approach for improved post-processing of CFH data, but because CFH acts as reference and cannot be validated against itself, it is presented only as supplementary information for the flight in which most instruments operated favorably, i.e., flight 30.

PCFH. During the course of the project, the PCFH instrument was continuously modified and further developed. Many exploratory modifications, such as the modulation of the reflectance setpoint to generate Golden Points in a predefined deterministic manner, were implemented in one of its sub-units (sub-unit 2). Therefore, only data from sub-unit 1 are displayed throughout. This sub-unit, similar to CFH, implements a fixed setpoint PID control scheme with residual non-equilibrium errors and non-deterministic Golden Points occurrences. As with the CFH, mirror-cleaning and condensate-reforming cycles were excluded from the data. Their onset was detected by the transition of the Peltier operation from cooling to heating, and their termination was identified when the optical signal settled within the prescribed control range. Data points with loss of control, indicated by optical signal values outside the control range and, e.g., in the case of insufficient cooling capacity, by the Peltier current being fixed at maximum cooling, were also rejected. Measurements were corrected for non-equilibrium (Poltera et al., 2026), i.e., the (scaled) mirror reflectivity was subtracted from the measured H_2O partial pressure, using RS41 radiosonde telemetry to estimate the morphological sensitivity of the mirror. The non-equilibrium corrected mirror temperature was converted to dew or frost point temperature, depending on the phase of the condensate. To compute the water vapor mixing ratio from the dew/frost point measurement, GNSS pressure from RS41 was used, as for CFH.

RALMO. At time t, the profile of water vapor mixing ratio $q(t, z)$ is retrieved from the Raman signals $S_{\mathrm{H_2O}}$, backscattered from the water vapor molecules, and $S_{\mathrm{N_2}}$, backscattered from the nitrogen molecules, to which it is proportional through their ratio $R = S_{\mathrm{H_2O}}/S_{\mathrm{N_2}}$ at the altitude z. Raw profiles of q, acquired at a native resolution of 1 min and 3.75 m, are averaged into $\overline{q}$ profiles at 45 min and 250 m resolution. When comparing $\overline{q}$ with collocated in-situ or remote sensing instruments, the 45 min averaging window starts at the launch time t_l of the balloon-attached in-situ instrumentation.

Several error sources contribute to the uncertainty budget of the retrieved q profile: the solar background, which introduces both a systematic and a random error in the raw signals; the uncertainty in the calibration factors; and the dead-time correction

https://doi.org/10.5194/egusphere-2026-7088
Preprint. Discussion started: 23 November 2026
© Author(s) 2026. CC BY 4.0 License.

of the acquisition system. The total uncertainty is obtained by Gaussian error propagation of these individual RALMO measurement uncertainties through the mixing ratio equation at altitude z and time t. Because this uncertainty depends on the state of the instrument and of the atmosphere, it can degrade the quality of the retrieval under conditions of high optical thickness (clouds, precipitation, high aerosol concentration). The q profile is automatically flagged and discarded whenever the SNR < 1.

RS41. The relative humidity is converted to H_2O mixing ratio according to Hardy's saturation vapor pressure formulation (Hardy, 1998) used by Vaisala. RS41 data are presented without flagging (except very dry values artificially clamped at 0.5%RH by the Vaisala software, which have been discarded). All in-situ instruments (ALBATROSS, PCFH and CFH) use air temperature, GNSS pressure and altitude data from RS41 to convert their primary measurements into vertically resolved profiles of water vapor mixing ratio.

Selected vertical profiles of H_2O mixing ratio from the surface to 35 km are shown on Figure 7. Overall, the profiles consistently show the expected decrease in H_2O mixing ratio with altitude, with most instruments capturing the same major moist and dry layers. The flight selection is characterized by important differences in the configuration and number of available instruments. Hence, each flight should be considered separately. In the Appendix B figures, the altitude layers where clouds were present during the ascent of the payloads are marked by gray shaded areas.

In flight 30, the CFH is shown both as processed by the regular procedure for this instrument (green) and as the same data processed using the newly developed Golden Points and non-equilibrium post-processing analysis (Poltera et al., 2021, 2026), down-sampled to 250 m vertical resolution (see CFH GP asc/dsc traces in Fig. 7).

Flight-dependent differences between the instruments are observed, particularly in the very dry upper troposphere and in layers with strong vertical gradients, whereas the agreement is closest in the humid lower troposphere, as can be seen in the per-flight profiles of Appendix B. The deviations are partly explained by atmospheric variability and partly by flight-specific factors, such as potential contamination from the ascending balloons and the payload configurations.

The operational radiosondes, in particular RS41 with heating capability (e.g., Romanens et al. (2026)), provide valuable auxiliary information on the atmospheric structure and generally reproduce the bulk tropospheric profile, agreeing with CFH to $-0.1 \pm 4.1\%$ over 0–12 km. The RS41 radiosonde is not considered for the stratosphere, the mean difference to CFH over 12-28 km being $+67.6 \pm 113.6\%$.

For the statistical comparison, all flights that provided valid PCFH or ALBATROSS measurement data were considered, i.e., the flights 2, 13, 17, 19–22, 25, 29–32. For PCFH, only the flights performed since January 2025 (i.e., from flight 18 onwards) are selected as valid, due to major technical rearrangements performed on the instrument at this time (see Section 2.2.2). These include a total of 9 flights: 19–22, 25, 29–32. For ALBATROSS, all 6 performed flights are included: 2, 13, 17, 19, 20, and 30. These include both co-located and tandem flights, i.e., flights in which the CFH instrument was flown either on the same or a separate balloon from ALBATROSS (see Table A1). RALMO participated in 9 of these flights: 2, 17, 19–22, 30–32. The profiles are shown in Figures B1 and B2.

For each dataset, the processing and flagging are done individually for each instrument. The differences are calculated by first binning the mixing ratio ($\frac{p_{H_2O}}{p}$) data onto a fine altitude grid with a spacing of 25 m to obtain a common altitude grid between the different retrievals. Then, the difference on the common grid between the respective instrument and CFH is calculated, and

https://doi.org/10.5194/egusphere-2026-7088
Preprint. Discussion started: 23 November 2026
© Author(s) 2026. CC BY 4.0 License.

subsequently binned onto a coarser grid with a spacing of 250 m below 12 km and 500 m above. ALBATROSS is compared on both the ascent and the descent, whereas PCFH and RALMO are compared on the ascent only. Finally, the mean values and standard deviations across all flights (given in Table 2) are calculated using the averaged differences. Figure 8 presents the results of the statistical comparison over the full range of the instruments, including the number of flights per instrument and the number of points used. Each point is one flight's mean difference in one bin, with its horizontal error bar showing the standard deviation of the difference within that bin; the thick solid line is the mean across all flights and the thin solid lines the ± 1 standard deviation about it, both averaged over 2 km layers. These are unweighted pooled statistics over individual comparison points, not flight-weighted (i.e., flights with more data points contribute more).

The instrument availability varies between flights. ALBATROSS was not deployed on flights 21, 22, 25, 29, 31 and 32, because of unfavorable weather conditions and/or landing point prediction, and RALMO did not contribute to flights 13, 25 and 29; for flight 29 this was due to low stratus cloud and light precipitation that started at about 17 UTC and lasted till the following day. These flights served as testing and validation flights for PCFH against CFH, and provided useful insights and demonstrated once more the ability of PCFH to resolve most of the atmospheric features even in the presence of extended cloud layers (Figure B1).

For the statistical comparisons, we use all flights in which the instruments operated as expected. Instrument-specific data-processing procedures are applied to ensure data quality. Invalid data points are discarded and consequently not shown in the following figures according to the individual instrument criteria described above. The vertical profiles of every flight entering the statistical comparison are presented in Appendix B.

4.1 Tropospheric comparison

The flights selected for the tropospheric comparison were chosen to provide representative examples of instrument performance under conditions suitable for data quality assessment. This selection reflects configurations in which all instruments operated reliably and allow for a consistent assessment of their capabilities. In Figure 7, we present three representative profiles meeting the predefined data-quality criteria, involving all instruments for the profile comparison. These are the 1 s-resolution profiles for the ascent of flight 19 and both the ascent and the descent of flight 30. This selection ensures that each instrument is present in at least one panel.

Overall, the tropospheric comparison demonstrates the operational performance of the new instruments and the consistency across the different observing systems, as can be seen for every flight in Figures B1 and B2. The agreement between PCFH and CFH throughout the troposphere confirms the reliability of the Peltier-cooled frost point approach, while ALBATROSS demonstrated its capability to capture fine-scale atmospheric structures in the tropopause region. These results provide a basis for the subsequent analysis of the UTLS, where measurement uncertainties are larger.

https://doi.org/10.5194/egusphere-2026-7088
Preprint. Discussion started: 23 November 2026
© Author(s) 2026. CC BY 4.0 License.

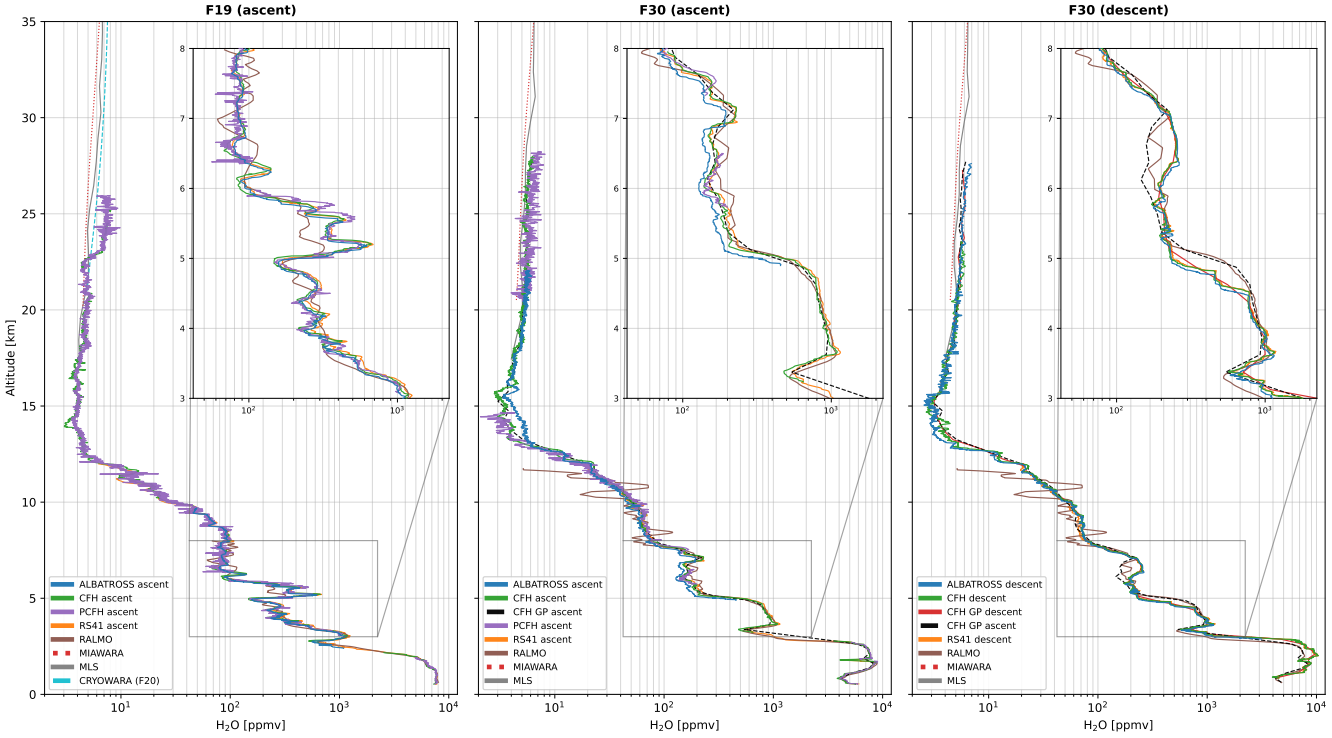

Figure 7. Selected vertical profiles of H_2O mixing ratio from the surface to 35 km. **Left to right**: Flight 19 ascent, Flight 30 ascent, and Flight 30 descent. In the troposphere, the available in situ and RALMO measurements consistently reproduce the principal vertical structures. The balloon-borne instruments resolve the transition across the tropopause and into the lower stratosphere, while MIAWARA and MLS extend the displayed coverage to higher altitudes. RALMO and RS41 are shown up to an altitude of 12 km, corresponding to the altitude range over which sufficiently reliable profiles were available. The microwave-radiometer retrievals are displayed above 20 km; below 35 km, they are mainly driven by a priori profiles and not measurements. The CRYOWARA profile from Flight 20 is included in the Flight 19 panel for illustration even though it is not temporally coincident. Insets show the 3–8 km range on a common mixing-ratio scale.

Over the entire troposphere (0–12 km), ALBATROSS agrees with the CFH within a small overall negative bias of $-1.3 \pm 6.1\%$ (N = 236 points from six flights) and 89.4 % of the observations falling within $\pm 10\%$. The agreement remains highly consistent across the upper troposphere ($-1.7 \pm 6.1\%$, 8–12 km) and free troposphere ($-1.2 \pm 6.4\%$, 4–8 km), indicating that the instrument performs robustly over a wide range of humidity conditions. In the lower troposphere, the agreement is closest ($+0.1 \pm 2.3\%$, 0–4 km), while part of the variability at higher altitudes can be attributed to representativeness errors associated with the tandem flight configuration, as the two payload instruments sampled air masses that increasingly diverged with altitude (Brunamonti et al., 2026). For the flight-to-flight weighted case, the mean bias over the full troposphere is $-1.6 \pm 2.9\%$, close to the point-weighted value, but with a considerably smaller scatter. This further indicates that the observed bias is reproducible from flight to flight and that the remaining variability is dominated by within-flight atmospheric effects rather than systematic instrumental offsets. The observed level of agreement is comparable to that achieved among established research-

https://doi.org/10.5194/egusphere-2026-7088
Preprint. Discussion started: 23 November 2026
© Author(s) 2026. CC BY 4.0 License.

grade hygrometers in recent laboratory and field intercomparison exercises (Brunamonti et al., 2025), supporting the suitability of ALBATROSS for high-resolution UTLS water vapor measurements.

For the same tropospheric range, the PCFH shows a mean bias of $0.1 \pm 6.4\%$ (N = 298 points from nine flights; 89.3% within $\pm 10\%$), with the smallest bias and the smallest scatter in the humid lower troposphere ($< 0.1\% \pm 2.3\%$, 0–4 km, N = 102), where all comparison points fall within $\pm 10\%$. The bias stays below 1% in magnitude at every other level as well, $+0.9\%$ in the free troposphere (4–8 km) and -0.3% in the upper troposphere (8–12 km), while the scatter grows steadily with altitude and is largest above 8 km ($\pm 7.9\%$). For the flight-to-flight weighted case, the mean bias is $-0.0 \pm 2.1\%$, close to the point-weighted value. Similar to ALBATROSS, the flight-to-flight standard deviation is much smaller than the point-to-point scatter, supporting the impact of atmospheric effects within the flights.

RALMO agrees with CFH to $+3.5 \pm 19.2\%$ over the full troposphere (N = 316 points from nine flights). The agreement between the altitude-resolved humidity profile of RALMO and the CFH strongly depends on altitude. The scatter is smallest below 4 km ($+1.5 \pm 10.2\%$), where the CFH sonde is not too far from the RALMO-probed atmospheric column, and grows steadily toward the tropopause ($+6.4 \pm 18.3\%$ between 4 and 8 km and $+2.1 \pm 28.6\%$ above 8 km) as the relative distance between RALMO and the CFH increases. The moist bias is most pronounced in the free troposphere, where the flight-to-flight weighted value of $+6.3 \pm 4.4\%$ over nine flights is large compared with its flight-to-flight spread, indicating that RALMO provides moister values than the CFH in that layer. Above 8 km the flight-weighted bias is $+1.7 \pm 11.7\%$ across the six contributing flights, so what dominates there is the scatter rather than a systematic offset. The growth of the scatter with altitude can be related to an overall drop in the signal-to-noise ratio of the RALMO signal, together with representativeness errors arising from atmospheric variability and the increasing horizontal separation between the ascending balloon and the lidar beam close to the tropopause.

https://doi.org/10.5194/egusphere-2026-7088
Preprint. Discussion started: 23 November 2026
© Author(s) 2026. CC BY 4.0 License.

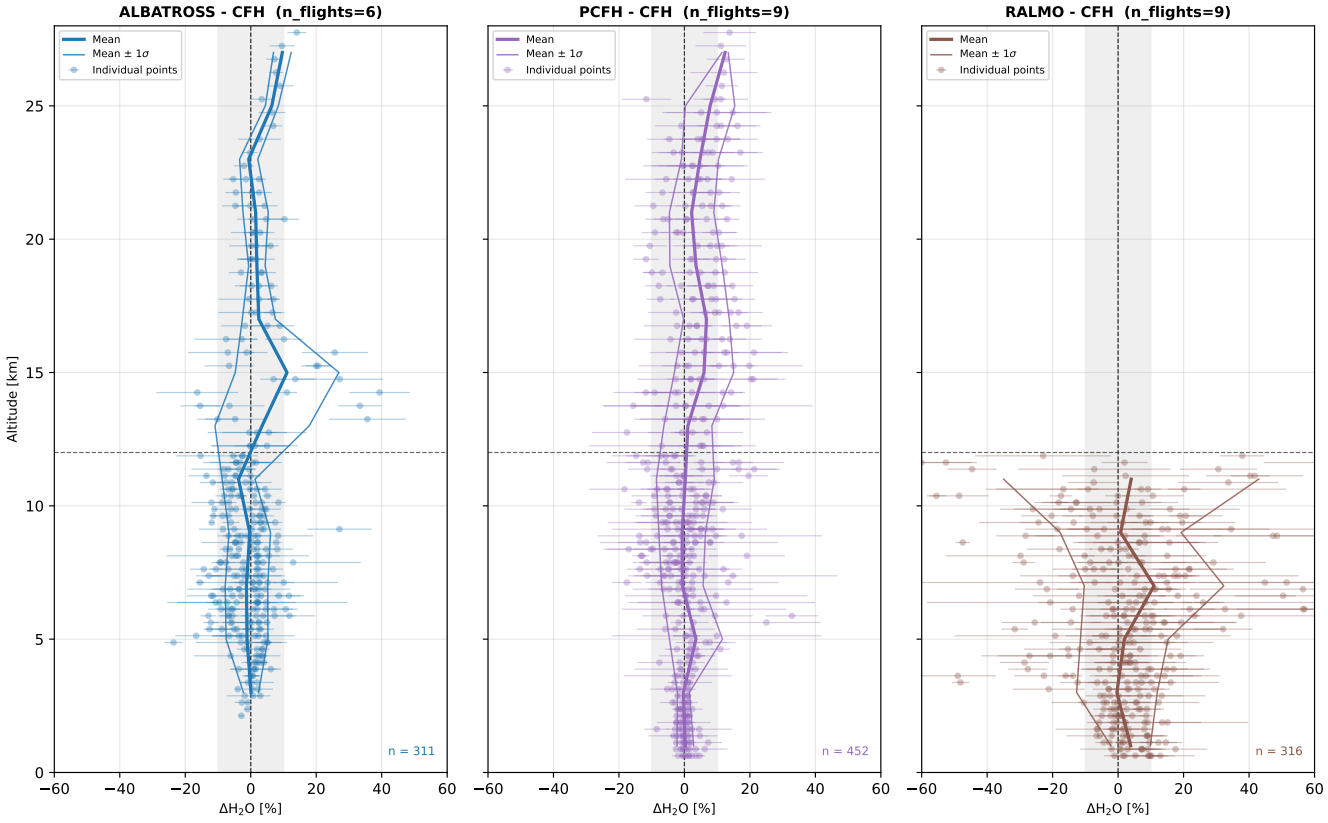

Figure 8. Statistical comparison: relative difference in H_2O mixing ratio between CFH and the participating instruments (ALBATROSS, PCFH and RALMO) over the full profile of 0–28 km. The gray band marks the $\pm 10\%$ agreement level, and the number of contributing flights and comparison points is given in each panel. The dotted horizontal lines indicate the 12 km limit.

https://doi.org/10.5194/egusphere-2026-7088
Preprint. Discussion started: 23 November 2026
© Author(s) 2026. CC BY 4.0 License.

Table 2. Comparison summary of ALBATROSS, PCFH and RALMO with the CFH reference over the full available range, and of the two CFH cooling configurations (R23 versus DIA) with each other. N is the number of per-flight, per-bin comparison points; the mean bias is their mean relative difference with respect to CFH, Std is their standard deviation, and RMS is the root-mean-square of the relative differences, which combines bias and scatter. The bins are 250 m below 12 km and 500 m above. RALMO is a tropospheric instrument and is discarded above 12 km. The number of contributing flights differs between the troposphere and the stratosphere and is given on the summary row of each region.

Comparison	Altitude range	N	Mean bias	Std	RMS	Within $\pm 10\%$	Within $\pm 20\%$
ALBATROSS − CFH	Troposphere (0–12 km, 6 flights)	236	-1.3%	6.1%	6.2%	89.4%	99.2%
	Lower trop. (0–4 km)	21	+0.1%	2.3%	2.3%	100.0%	100.0%
	Mid trop. (4–8 km)	118	-1.2%	6.4%	6.6%	85.6%	99.2%
	Upper trop. (8–12 km)	97	-1.7%	6.1%	6.3%	91.8%	99.0%
	Stratosphere (12–28 km, 4 flights)	75	+4.1%	9.9%	10.8%	80.0%	92.0%
	Lower strat. (12–20 km)	49	+4.7%	11.7%	12.6%	73.5%	87.8%
	Mid strat. (20–28 km)	26	+3.0%	4.8%	5.7%	92.3%	100.0%
PCFH − CFH	Troposphere (0-12 km, 9 flights)	298	0.1%	6.4%	6.4%	89.3%	99.0%
	Lower trop. (0–4 km)	102	<0.1%	2.3%	2.3%	100.0%	100.0%
	Mid trop. (4–8 km)	83	+0.9%	7.3%	7.4%	86.7%	97.6%
	Upper trop. (8–12 km)	113	-0.3%	7.9%	7.9%	81.4%	99.1%
	Stratosphere (12–28 km, 7 flights)	154	+4.6%	7.7%	9.0%	69.5%	98.1%
	Lower strat. (12–20 km)	93	+4.5%	8.2%	9.4%	68.8%	96.8%
	Mid strat. (20–28 km)	61	+4.9%	6.9%	8.4%	70.5%	100.0%
RALMO − CFH	Troposphere (0-12 km, 9 flights)	316	+3.5%	19.2%	19.6%	59.8%	82.0%
	Lower trop. (0–4 km)	120	1.5%	10.2%	10.3%	78.3%	95.8%
	Mid trop. (4–8 km)	119	+6.4%	18.3%	19.4%	51.3%	77.3%
	Upper trop. (8–12 km)	77	2.1%	28.6%	28.7%	44.2%	67.5%
R23 − DIA	Troposphere (0-12 km, 9 flights)	252	+0.5%	2.0%	2.0%	98.8%	100.0%
	Lower trop. (0–4 km)	108	+0.6%	1.2%	1.3%	99.1%	100.0%
	Mid trop. (4–8 km)	94	+0.6%	2.0%	2.1%	98.9%	100.0%
	Upper trop. (8–12 km)	50	+0.1%	2.9%	2.9%	98.0%	100.0%
	Stratosphere (12–28 km, 9 flights)	55	-0.7%	9.8%	9.8%	72.7%	94.5%
	Lower strat. (12–20 km)	37	-0.2%	10.2%	10.2%	70.3%	94.6%
	Mid strat. (20–28 km)	18	-1.7%	8.7%	8.9%	77.8%	94.4%

https://doi.org/10.5194/egusphere-2026-7088
Preprint. Discussion started: 23 November 2026
© Author(s) 2026. CC BY 4.0 License.

Besides the comparison of the new instruments against the CFH reference, the Swiss H_2O Hub campaigns provided a unique opportunity to evaluate CFH operated with the conventional R23 refrigerant against the alternative dry-ice/alcohol (DIA) cooling configuration. Direct comparison of the instruments using the same payload was achieved for nine flights. Because several soundings were affected by partial R23 cryogen loss, not all flights provided valid measurement profiles throughout the full atmospheric column. Figure B5 therefore highlights flight 27, which offers one of the most complete profile comparisons, both ascent and descent. For the statistical comparison, all flights with valid data from both configurations are used, and the results are presented in Figure B6 and in Table 2.

Since both hygrometers share the same radiosounding, altitude grid, and atmospheric sampling volume, the comparison is largely free from atmospheric representativeness uncertainties that affect intercomparisons between independent payloads. The high-resolution relative difference is therefore evaluated directly, point by point, without any prior binning. These values are then aggregated into the same coarser altitude bins used above. As above, these are unweighted pooled statistics over the individual per-flight, per-bin comparison points, not flight-weighted.

Across the troposphere (0–12 km), the two instruments are essentially identical, exhibiting an overall agreement of $+0.5 \pm 2.0\%$ (N = 252 points from nine flights), with 98.8% of points falling within $\pm 10\%$. The small and nearly altitude-independent bias ($\leq 0.6\%$) indicates that replacing R23 with the DIA-cooling mixture does not measurably affect frost point determination or mirror-temperature accuracy. The behavior of the two configurations above the tropopause, where the cooling system is under greater demand, is addressed in Section 4.2.

4.2 UTLS comparison

The UTLS is the primary target region of several instrument developments presented in this work, but it also remains the most challenging atmospheric region for water vapor observations. Water vapor mixing ratios decrease to only a few ppm, strong vertical gradients occur near the tropopause, and contamination effects can become comparable to the atmospheric signal itself. It is also the transition region between the upper boundary of the retrieval range of the ground-based lidar RALMO and the lower boundary of the retrieval range of the ground-based microwave radiometer MIAWARA (see Figure 1), and the altitude range in which the newly developed in-situ instruments are expected to improve the observations, filling the gap in existing remote sensing datasets. In contrast to the troposphere, the much drier air and the sharp vertical gradients provide a more demanding and more informative test of instrumental performance. Consequently, the number of profiles that satisfy the strict quality criteria adopted within the Swiss H_2O Hub is smaller than in the troposphere: 13, 17, 20 and 30 for ALBATROSS, and 19, 21, 22 and 29–32 for PCFH, shown in Figures B3 and B4. The RALMO data is discarded above 12 km, as its SNR < 1. The number of profiles available in the UTLS therefore remains smaller than in the troposphere, but it is sufficient for a first quantitative assessment of the performance reached in this region.

Flight 19 was chosen to demonstrate the capabilities of PCFH. The instrument follows CFH closely in the dry lower stratosphere, while above 22 km, both show a sudden increase in H_2O. This increase is consistent with the positive stratospheric water vapor anomaly following the Hunga Tonga volcanic eruption (Wright et al., 2022), see discussion below. The radiometers MLS, CRYOWARA, and MIAWARA are shown alongside. The CRYOWARA profile presented belongs to flight 20 from

https://doi.org/10.5194/egusphere-2026-7088
Preprint. Discussion started: 23 November 2026
© Author(s) 2026. CC BY 4.0 License.

2025-07-01 and is only included for completeness. MIAWARA and CRYOWARA cannot capture this increase because of low sensitivity at this altitude. ALBATROSS data are not available for this flight above 10 km. It should be mentioned that the MLS profiles used are overpasses from 2025-03-19 (- 8 days) for flight 19 and 2026-04-16 (- 14 days) for flight 30. These are the closest dates to the actual flights and are used for completeness.

Flight 30 provides the most comprehensive stratospheric ALBATROSS dataset acquired within the Swiss H_2O-Hub project and therefore offers the clearest assessment of the instrument's capabilities in the UTLS. Both ascent and descent are shown in Figure 7, but external moisture sources (see Brunamonti et al. (2026)) contaminate the ascent, thus valid data extend only to about 22 km, whereas the descent provides a full vertical profile until 28 km. The descent therefore demonstrates the capability of ALBATROSS to resolve extremely dry atmospheric conditions, including tropopause water-vapor mixing ratios approaching 3 ppm and lower-stratospheric values of 4–6 ppm up to approximately 28 km altitude. Throughout this altitude range, ALBATROSS remains in close agreement with the CFH reference and accurately captures the vertical water-vapor profile. Note that the Golden-Point-analysis profile of CFH is also shown, providing a smoother binned profile reaching higher altitudes and illustrating the advantage of this new processing technique (Poltera et al., 2026).

The statistical comparison of Figure 8 and Table 2 is extended above the tropopause, following the same procedure as in the troposphere. For ALBATROSS, both the ascent and the descent of flight 30 are included, providing 53 of the 75 ALBATROSS comparison points. The statistics are therefore weighted towards a single flight, although its ascent and descent sample the air mass independently, and the 75 points are sufficient for a first quantitative assessment of the achievable performance above the tropopause. Over the full stratospheric range considered here (12–28 km), ALBATROSS agrees with the CFH within $+4.1 \pm 9.9\%$ (N = 75 points from 4 flights), with 80.0% of the points falling within $\pm 10\%$ and 92.0% within $\pm 20\%$. The agreement improves with altitude: between 12 and 20 km the mean bias is $+4.7 \pm 11.7\%$, while above 20 km it is $+3.0 \pm 4.8\%$ with 92.3% of the points within $\pm 10\%$ and all of them within $\pm 20\%$. The larger scatter in the lower part of the range is consistent with the challenge of resolving the sharp vertical gradients encountered across the tropopause transition layer, whereas a tighter agreement is observed above ~ 16 km altitude (Fig. 8). This indicates the ability of the laser spectrometer to resolve mixing ratios in the 3–6 ppm range, as already shown in the profile comparison of flight 30.

For the same altitude range, PCFH agrees with the CFH within $+4.6 \pm 7.7\%$ (N = 154 points from seven flights; 69.5% within $\pm 10\%$ and 98.1% within $\pm 20\%$). The bias is stable with altitude, $+4.5 \pm 8.2\%$ between 12 and 20 km and $+4.9 \pm 6.9\%$ above 20 km, while the scatter decreases towards the driest layers and all comparison points above 20 km fall within $\pm 20\%$. The scatter therefore narrows with altitude, in the same way as for ALBATROSS, and the retrieval of the lowest frost point temperatures across various seasons indicates that the cooling capacity of the Peltier system is not a limiting factor over this altitude range with the present configuration.

The same statistical treatment is applied to the comparison of the two CFH cooling configurations above the tropopause. A larger variability is observed in the UTLS, mainly due to the much lower frost point temperatures, which place greater demands on the cooling system and where differences in controller response become more evident. Nevertheless, the mean bias remains overall well-constrained below 2%. Between 12 and 20 km, the mean difference is small (-0.2%) but exhibits the largest scatter ($\pm 10.2\%$, 70.3% within $\pm 10\%$, N = 37 from three flights), consistent with the rapid humidity gradients and changing

https://doi.org/10.5194/egusphere-2026-7088
Preprint. Discussion started: 23 November 2026
© Author(s) 2026. CC BY 4.0 License.

instrument operating conditions encountered across the tropopause transition layer. Above 20 km, the mean difference remains small (-1.7%) and has reduced variability ($\pm 8.7\%$, 77.8% within $\pm 10\%$, N = 18 from three flights). Despite the small number of flights, the 55 points are sufficient for a first quantitative assessment of the achievable performance above the tropopause of this alternative cooling approach. Taken together with the tropospheric result, these findings indicate that the DIA cooling approach has the capability to reproduce conventional CFH measurements with high fidelity while substantially reducing the environmental footprint associated with R23-based soundings. The remaining differences are primarily linked to differences in controller response due to the reduced cooling reserve of the DIA system rather than to systematic errors in frost point retrieval, supporting its potential as a practical low-GWP alternative for future reference-quality balloon-borne water-vapor observations.

Beyond the intercomparison of the balloon-borne instruments, the UTLS is also where the in-situ and remote-sensing retrievals overlap. The overlapping region of balloon-borne measurements and microwave radiometer measurements is illustrated in Figure 9, where in-situ balloon measurements are displayed alongside remote sensing MLS retrievals. The CFH measurements are consistent with the increase in lower stratospheric H_2O over Switzerland following the January 2022 Hunga Tonga–Hunga Ha'apai (HTHH) volcanic eruption. Residual biases between frost point hygrometers and MLS are partially associated with a drift in the MLS 190 GHZ "sideband fraction", as discussed in e.g. Livesey et al. (2021). The CFH and PCFH measurements during flights 18 and 19 shown in Figure 9 confirm positive anomalies from streams of aged polar vortex air often observed by MLS during springtime over Switzerland. The air mass trajectory calculations shown in Figure B7 validate the polar vortex origin of the airmass on flight 19, likely enriched with 3 year aged HTHH water vapor. The decrease in MLS sample availability following the duty-cycling of the space-borne radiometer starting in May 2024 (Salawitch et al., 2025) can also be observed from Figure 9.

In Figure 9, the chilled mirror lower stratospheric measurements provide in-situ evidence of post-Hunga Tonga seasonal variability over the Alpine region, supporting the variability observed in MLS overpass retrievals in this region.

https://doi.org/10.5194/egusphere-2026-7088
Preprint. Discussion started: 23 November 2026
© Author(s) 2026. CC BY 4.0 License.

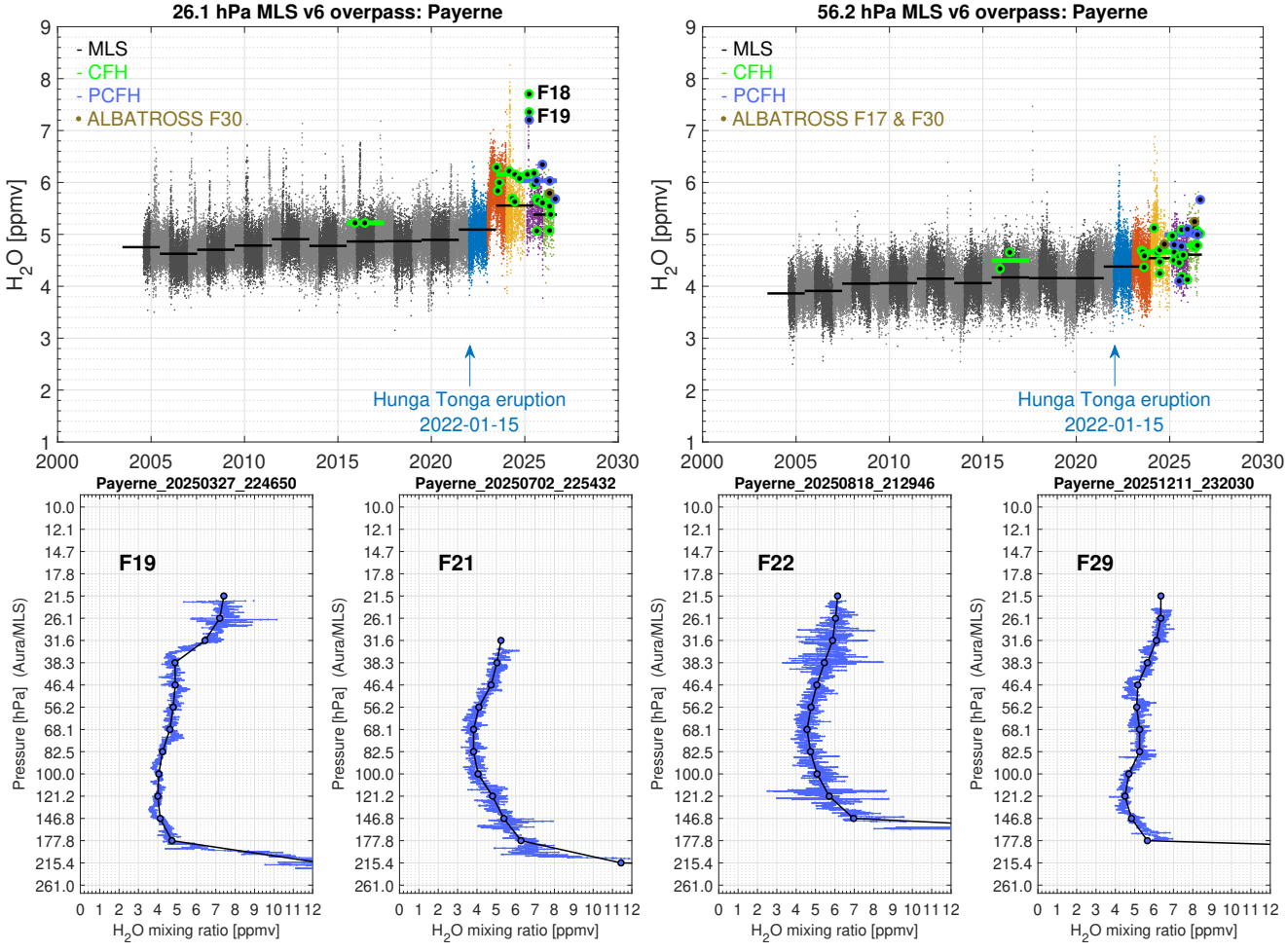

Figure 9. Top: Timeseries of H_2O mixing ratio retrieved from MLS overpasses over Payerne at two selected UTLS pressure levels of 56.2 hPa and 26.1 hPa (about 20 km and 25 km altitude, respectively), together with in-situ measurements (colored circles) at the same pressure levels. Prior to 2022, individual years are displayed in varying shades of gray, whilst starting in 2022, each year is assigned a distinct color. The CFH, PCFH and ALBATROSS observations (mixing ratio medians calculated over ±1 MLS pressure bins) at the corresponding pressure levels are superposed as green, blue and brown circles, respectively. The CFH observations are a combination of flights from Payerne (Swiss H_2O Hub) and Zurich (ETH test flights). The black, green and blue horizontal lines represent successive ±1 y MLS, CFH and PCFH measurement medians. Bottom: Vertical profiles of H_2O measured with PCFH during selected flights in 2025, covering early spring, mid-summer, late fall and early winter. The high-resolution data (blue dots) are overlaid with medians (black line with blue-filled circles) calculated over ±1 MLS pressure bins. The labels F19-F29 refer to the flights as specified in Table A1.

4.3 Middle-Atmospheric comparison

CRYOWARA observations were available during only one of the balloon campaigns listed in Table A1, because the instrument was still operated as a laboratory breadboard during most of the project. During the second breadboard phase, the instrument

https://doi.org/10.5194/egusphere-2026-7088
Preprint. Discussion started: 23 November 2026
© Author(s) 2026. CC BY 4.0 License.



was deployed outdoors for its first validation measurements. Figure 10 shows the water vapor profile retrieved on 18 December 2025 for which MLS data were available during an overpass near Bern. For comparison with the ground-based retrievals of MIAWARA and CRYOWARA, the MLS profile was convolved with the averaging kernel of each ground-based instrument. This accounts for the altitude-dependent vertical sensitivity and coarser effective resolution of the ground-based radiometers, approximately 12–19 km, and allows the profile differences to be evaluated at comparable vertical resolution. The comparison shows a good overall agreement between the three instruments, with differences generally on the order of 1 ppmv and a slightly better agreement between MLS and CRYOWARA at higher altitudes. In terms of relative differences, both instruments agree within $\pm 10\%$ with MLS between roughly 30 and 60 km, while CRYOWARA remains within $\pm 10\%$ over a considerably wider range, from about 35 up to 70 km. This is consistent with the improved sensitivity of CRYOWARA, which is expected to better resolve water vapor variations in the upper part of the retrieval range. The better agreement of CRYOWARA with MLS is explained by its measurement response (the sum of the corresponding row of the averaging kernel matrix, i.e. the fraction of the retrieved value at that altitude that originates from the measurement rather than from the a priori), which exceeds 0.8 (the threshold above which the retrieval is taken to be dominated by the measurement) over a wider altitude region (about 34–68 km) than that of MIAWARA (about 40–64 km). The differences are likely due primarily to location mismatch with the MLS measurement. MIAWARA has demonstrated that the overall agreement between MIAWARA and MLS between 30–70 km remains within $\pm 10\%$, (Bell et al., 2025b). However, it should be noted that the CRYOWARA retrieval algorithm is still largely based on the current MIAWARA setup and has not yet been fully optimized for the new instrument.

https://doi.org/10.5194/egusphere-2026-7088
Preprint. Discussion started: 23 November 2026
© Author(s) 2026. CC BY 4.0 License.

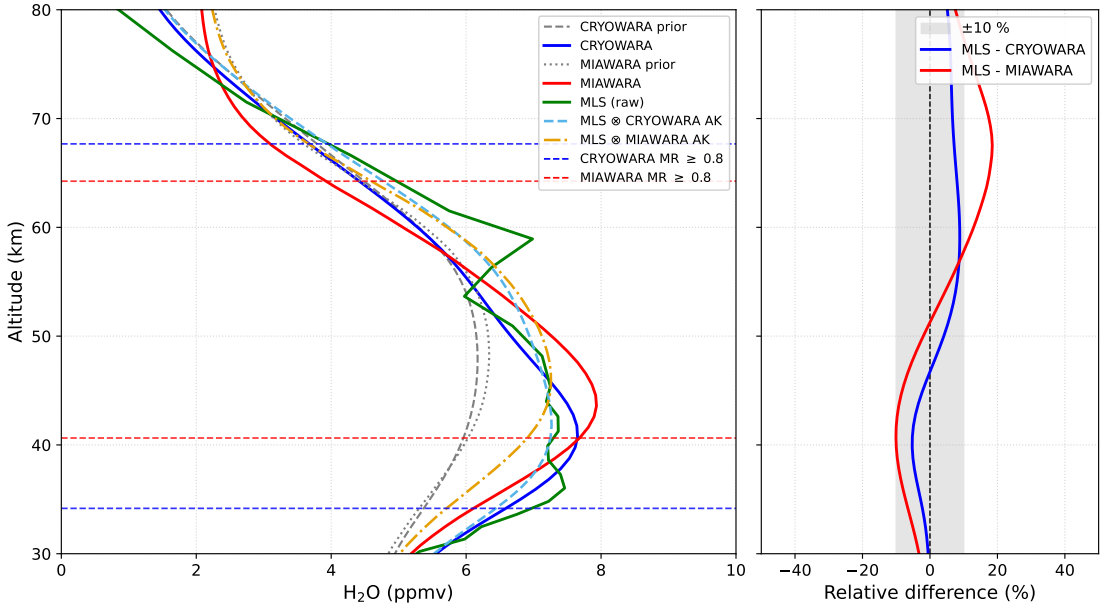

Figure 10. Comparison of retrieved H_2O profiles from CRYOWARA, MIAWARA, and MLS for 18 December 2025. Left: retrieved H_2O profiles (AK = averaging kernel; MR = measurement response). Right: relative differences between MLS and the two ground-based radiometers.

The significance for the continuation of the middle-atmospheric water vapor retrievals is highlighted by the observations of MIAWARA following the Hunga Tonga–Hunga Ha'apai (HTHH) eruption in 2022. The water vapor anomaly was observed in Switzerland in mid 2022, peaking from the end of 2024 to January 2025, as observed by MIAWARA (Bell et al., 2025a) and MLS. Figure 11 presents the time series of the H_2O measured at Zimmerwald relative to its day-of-year climatology.

https://doi.org/10.5194/egusphere-2026-7088
Preprint. Discussion started: 23 November 2026
© Author(s) 2026. CC BY 4.0 License.

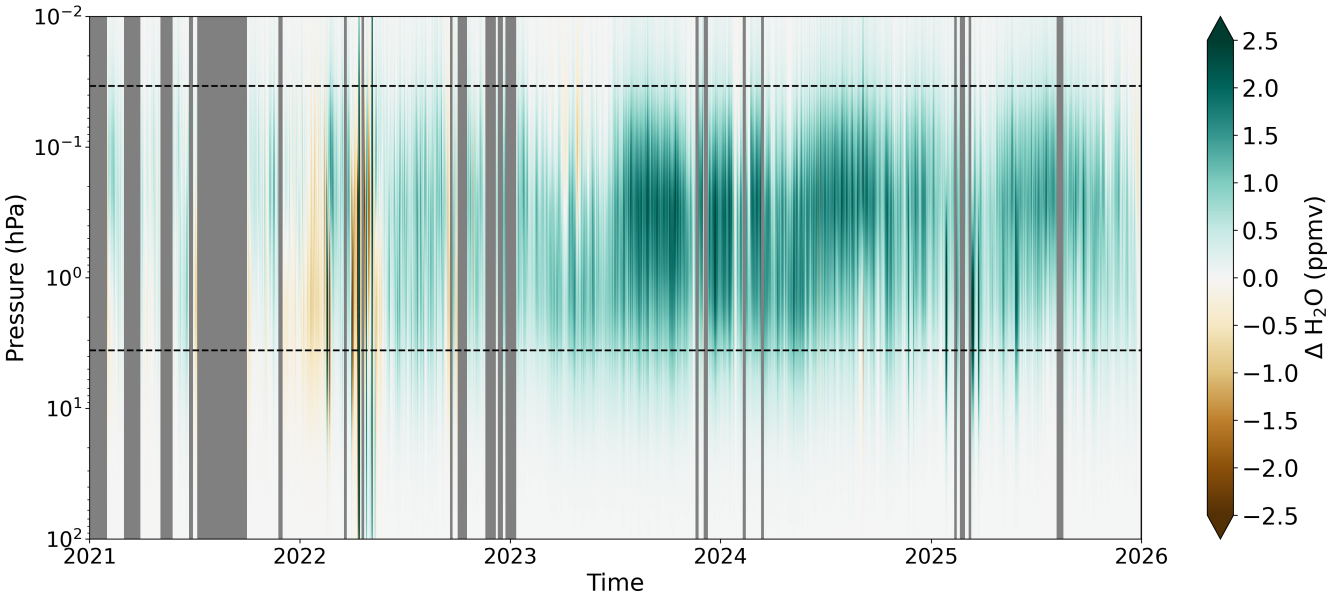

Figure 11. Water vapor anomaly post-HTHH (early 2022) w.r.t. pre-HTHH baseline, above the Zimmerwald observatory, as observed by MIAWARA. Differences of measured H_2O over the years, with a noticeable increase after 2023. The gray shaded areas represent measurement gaps due to maintenance. In 2021, MIAWARA underwent a major upgrade (Bell et al., 2025b). The dashed lines represent the region where the measurement response exceeds 0.8.

4.4 Ground to space

The vertical profiles in Figure 12 combine the best-performing measurement from each participating instrument. The MLS profiles for the two flights are included to illustrate the complementary altitude coverage and should not be interpreted as temporally coincident validation profiles. The only CRYOWARA profile available from the campaign period is from 2025-07-01, flight 20; it is included for completeness, although the radiometer was still in its breadboard phase (Filinis et al., 2026). Middle-atmospheric H_2O varied little over these dates, so the retrievals remain consistent between the two ground-based radiometers.

https://doi.org/10.5194/egusphere-2026-7088
Preprint. Discussion started: 23 November 2026
© Author(s) 2026. CC BY 4.0 License.

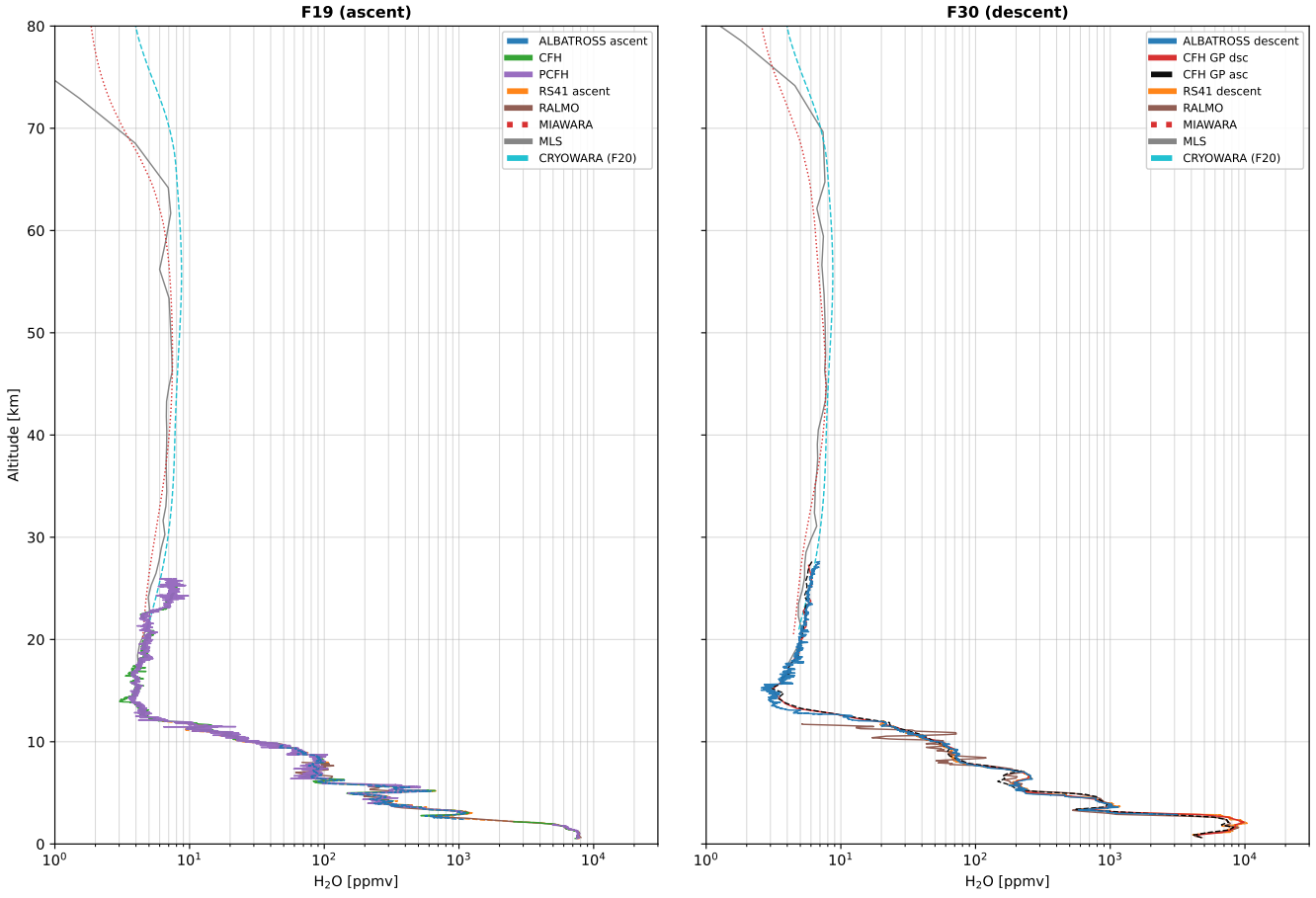

Figure 12. Composite water-vapor profiles from ground-to-space obtained with the Swiss H_2O Hub observing systems. The panels combine measurements associated with Flight 19 ascent (left) and Flight 30 descent (right). Balloon-borne instruments and RALMO resolve the tropospheric structure and the sharp decrease in water-vapor mixing ratio across the tropopause up to the UTLS, while MIAWARA and MLS extend the altitude coverage into the middle atmosphere at coarser vertical resolution. The CRYOWARA profile, available for Flight 20, is included to indicate the coverage of the new radiometer and is not temporally coincident with the displayed flights. The composite profiles demonstrate the complementary and overlapping altitude ranges of the participating measurement techniques rather than a simultaneous full-column intercomparison.

5 Discussion

The Swiss H_2O Hub lays the groundwork for high-accuracy H_2O measurements from the surface to the mesopause with a new generation of co-located and vertically overlapping in-situ and remote sensing instruments. An important outcome is the establishment of observational traceability across atmospheric regions that are traditionally monitored by separate communities

https://doi.org/10.5194/egusphere-2026-7088
Preprint. Discussion started: 23 November 2026
© Author(s) 2026. CC BY 4.0 License.

and techniques. Rather than considering individual instruments as independent measurement systems, the campaign results support a hierarchical observing strategy in which each technique contributes according to its strengths.

The intercomparison demonstrates the in-flight capabilities of both newly developed in-situ balloon-borne instruments, PCFH and ALBATROSS, to provide accurate measurements of H_2O mixing ratio data, consistent with the CFH reference throughout the entire measurement column. The observed differences between the instruments (see Table 2) are generally of the same order as the uncertainty assigned to reference-quality CFH itself, indicating that the remaining discrepancies are increasingly constrained by reference uncertainty and atmospheric representativeness rather than by systematic instrumental biases.

ALBATROSS successfully resolved H_2O mixing ratios of only a few ppm in the UTLS region, and reached its closest agreement with CFH in the lower and middle stratosphere ($\sim 16 - 28$ km altitude). This level of performance is comparable to the agreement reported among leading research hygrometers (Vömel et al., 2007; Hall et al., 2016) during recent field and laboratory intercomparisons, including the AquaVIT exercises (Fahey et al., 2014; Brunamonti et al., 2025). Together with its SI traceability, high precision, and rapid dynamic response (see Brunamonti et al. (2026)), these results demonstrate that mid-infrared laser absorption spectroscopy represents a viable approach for reference-quality balloon-borne measurements of UTLS water vapor. These findings are particularly valuable because they are based on a fundamentally different measurement principle than frost point hygrometry.

The PCFH matured from a research prototype to an industrial-grade instrument during the project, while maintaining close agreement with CFH over a wide range of atmospheric conditions. The results indicate that the transition from cryogenic to Peltier-based cooling can be achieved without compromising measurement quality, thereby addressing a major challenge facing the future of operational frost point hygrometry after the phase-out of R23 refrigerant with a fully-electric dual inlet design. This holds throughout the UTLS as well: the agreement with CFH does not degrade towards the lowest frost point temperatures encountered up to 28 km, the mean bias staying near $+4.6\%$ from the tropopause upwards, so the available cooling capacity of the Peltier system compared to R23 refrigerant is not a limiting factor over the altitude range sampled here. The successful deployment of DIA-CFH further strengthens this conclusion. Although slightly heavier than the conventional CFH, the 1.5 kg PCFH still allows the entire payload to stay well below the aviation safety limits. Through Peltier cooling, the logistical efforts are minimal and flight preparation is fast and straightforward. It can be launched out of the box within half an hour. With its dual inlet design and asynchronous cleaning cycles, it has the ability to provide continuous vertical profiles and a lower likelihood of contamination in the stratosphere compared to CFH, combined with the ability to detect it. In future applications, with onboard pressure and GNSS measurements, ambient air temperature measurement, and cross-validating dual inlet design, it will gain the ability to autonomously perform the non-equilibrium correction of its frost point measurement data and compute the water vapor mixing ratio without the use of additional radiosonde telemetry.

The intercomparison with RALMO highlights both the strengths and limitations of combining in-situ and remote sensing observations. In the lower and middle troposphere, the good agreement (< 6.4 %) between CFH and RALMO confirms the ability of the lidar to provide continuous monitoring of atmospheric humidity while remaining anchored to reference-quality balloon observations. This capability is particularly valuable because it bridges the temporal gaps between individual balloon launches

https://doi.org/10.5194/egusphere-2026-7088
Preprint. Discussion started: 23 November 2026
© Author(s) 2026. CC BY 4.0 License.

and provides information on moisture variability at timescales inaccessible to campaign-based measurements. Deterioration/-growth of the scatter towards the tropopause should not be interpreted solely as an instrumental limitation. At these altitudes, the ascending balloon may sample air masses tens of kilometers away from the lidar beam, while atmospheric humidity gradients become larger and signal-to-noise ratios decline. As a consequence, representativeness errors arising from differences in sampling volume become increasingly important. The observed discrepancies therefore reflect not only measurement uncertainty but also the inherent challenge of comparing a quasi-Lagrangian in-situ observation with a fixed-column remote sensing measurement in a dynamically active region of the atmosphere. The comparison also evidences the complementary nature of the observing techniques. RALMO provides continuous temporal coverage but becomes progressively constrained at higher altitudes. In contrast, the balloon-borne hygrometers maintain high vertical resolution and sensitivity throughout the UTLS, albeit at limited temporal sampling. The agreement observed in their overlap region demonstrates that these techniques are most powerful when used together rather than independently.

DIA-CFH has been demonstrated to be a suitable alternative to the traditional CFH that uses R23 for the measurement of the atmospheric frost point up to about 28 km, using a low-GWP cryogenic mixture. Unlike the comparisons with the other instruments, this inter-comparison is not affected by atmospheric representativeness: both configurations are the same probe flown on the same payload, sampling the same air at the same time, so the observed differences can be attributed to the cooling system and its control alone. The reported numbers are therefore not directly comparable to the instrument-versus-CFH statistics, in which in some of the flights the two instruments sample increasingly different air masses with altitude. The two configurations agree closely, with a mean bias of about 0.5% in the troposphere and below 2% in the stratosphere. The agreement is closest in the troposphere, while in the stratosphere, the variability increases to about 10% due to differences in PID-control response between the two types of cryogen, especially across the tropopause transition layer. There is also a residual risk of losing frost control when the second cleaning cycle (automatically triggered at -53°C frost point, typically above 8 km) occurs above the tropopause, which occurred on 3 out of 26 occasions over Payerne. To minimize such a risk, DIA-CFH may benefit from a triggering at higher temperature of the cleaning cycle procedure.

At higher altitudes, the coordinated operation of MIAWARA, CRYOWARA, and MLS establishes continuity between regional ground-based monitoring and global satellite observations. While balloon-borne instruments provide detailed information up to approximately the lower stratosphere, microwave radiometry extends the observational record into the middle atmosphere, where long-term variability is closely linked to transport and dynamical processes. The development and first deployment of CRYOWARA represent an important step towards ensuring the continuity of Swiss middle-atmospheric water-vapor observations. Although the instrument remained in a validation phase during the campaign period, the initial comparisons with MIAWARA and MLS demonstrate consistency with the existing observing system and confirm the expected benefits of cryogenic receiver technology.

Several limitations should be considered when interpreting the presented results. Both ALBATROSS and PCFH underwent iterative development during the campaign period, such that successive flights often correspond to progressively improved instrument versions. Consequently, the reported performance reflects not only instrument validation but also instrument maturation. Furthermore, the number of available stratospheric intercomparisons remains limited for ALBATROSS, where stringent

https://doi.org/10.5194/egusphere-2026-7088
Preprint. Discussion started: 23 November 2026
© Author(s) 2026. CC BY 4.0 License.

flying requirements and contamination issues restricted the number of flights and the coverage of usable UTLS profiles, with a single sounding providing the majority of the valid comparison points. For the remote sensing observations, temporal and spatial collocation remains an important limitation. MLS overpasses are not always coincident with the balloon campaigns, and only a very limited number of CRYOWARA retrievals were available during the balloon validation phase. Despite these limitations, the campaign has established a robust foundation for future integrated observing systems. Continued instrument development, coordinated intercomparison flights, and long-term operation of the observing network revealed the potential to further strengthen the traceability and continuity of water-vapor observations across the atmospheric column.

6 Conclusions

The Swiss H_2O Hub project was established to strengthen vertically resolved measurements of atmospheric water vapor across the troposphere, stratosphere, and mesosphere by combining complementary in-situ and remote sensing techniques. Over the course of the project, coordinated campaigns comprising 43 balloon launches were conducted from Payerne, accompanied by continuous observations using ground-based lidar and microwave radiometers. These measurements enabled the evaluation of novel technologies against established reference instruments and the investigation of observational consistency across different atmospheric regions. Moreover, the campaign data facilitated the identification and mitigation of key technical issues, including contamination effects in ALBATROSS and challenges related to cooling, temperature control, and calibration in PCFH, thereby substantially advancing their operational readiness.

Throughout the troposphere, the campaign results demonstrate that the newly developed balloon-borne hygrometers ALBATROSS and PCFH achieve close agreement with the CFH reference. ALBATROSS achieved a mean agreement of $-1.3 \pm 6.1\%$ over six flights, while PCFH agreed within $+0.1 \pm 6.6\%$ over nine flights. These results confirm that both instruments are able to resolve the vertical structure of atmospheric water vapor with an accuracy comparable to established state-of-the-art techniques.

The project further demonstrated the feasibility of environmentally sustainable alternatives to conventional cryogenic frost point hygrometry. The electrically cooled PCFH reproduced CFH observations within the uncertainty of the reference instrument, while the DIA-CFH configuration showed that low-GWP cryogenic cooling can provide measurements that are consistent with the conventional CFH in both the troposphere and stratosphere. Together, these developments represent important progress towards maintaining reference-quality UTLS humidity observations in a post-R23 environment.

Despite substantial progress, the UTLS remains one of the least constrained regions of the atmosphere for water vapor observations. Above the tropopause, both new instruments nevertheless reach a quantitative level of agreement with the CFH reference: $+4.1 \pm 9.9\%$ for ALBATROSS and $+4.6 \pm 7.7\%$ for PCFH between 12 and 28 km in 500 m bins; above 20 km, all comparison points fall within $\pm 20\%$ (see Table 2). Considering CFH's inherent uncertainties, this qualifies the data of both instruments as useful for climate-monitoring studies. The presented results therefore represent an important step towards improved UTLS monitoring and a first quantitative assessment of both instruments above the tropopause. At the same time, it

https://doi.org/10.5194/egusphere-2026-7088
Preprint. Discussion started: 23 November 2026
© Author(s) 2026. CC BY 4.0 License.

highlights both the difficulty of acquiring reference-quality measurements in this region and the continued need for coordinated observational efforts.

The long-term observing component of the Swiss H_2O Hub was strengthened through the continued operation of RALMO and MIAWARA and the development of the next-generation radiometer CRYOWARA. RALMO provided continuous high-resolution measurements of tropospheric humidity, complementing the balloon-borne observations with substantially improved temporal sampling. In the middle atmosphere, the first comparisons between CRYOWARA, MIAWARA, and MLS demonstrate agreement within approximately 10% over the altitude range from 30 to 70 km and provide encouraging evidence that CRYOWARA will ensure continuity of the Swiss middle-atmospheric water-vapor record while improving sensitivity and temporal resolution. Taking the difference with respect to MLS as an indicative measure, the retrievals agree to within 0.2–0.5 ppmv over the mid-mesosphere, comparable to the "breakthrough-to-threshold" levels, degrading to 0.7–0.8 ppmv towards the edges of the sensitive range.

The coordinated observations demonstrate that complementary balloon-borne, ground-based, and satellite-based techniques can be linked through overlapping altitude coverage to provide a consistent view of atmospheric water vapor from the lower troposphere to the mesosphere. The resulting observational framework enables cross-validation between independent measurement principles and establishes traceability across atmospheric regions that are traditionally observed by separate systems. Beyond the evaluation of individual instruments, the Swiss H_2O Hub therefore demonstrates the feasibility of an integrated water-vapor observing system capable of supporting long-term, climate-quality observations of one of the most important atmospheric constituents.

https://doi.org/10.5194/egusphere-2026-7088
Preprint. Discussion started: 23 November 2026
© Author(s) 2026. CC BY 4.0 License.

Appendix A: List of campaign flights

Table A1. Summary of the Swiss H_2O Hub flights (100% payload and data recovery).

Flight N_o	Date & Time	Balloon #1	Balloon #2	Remote sensing
1	2023-08-15, 22 LT	PCFH, CFH	None	MIAWARA, RALMO
2	2023-08-17, 23 LT	PCFH, CFH	ALBATROSS	MIAWARA, RALMO
3	2023-08-22, 22 LT	PCFH, CFH	None	MIAWARA, RALMO
4	2023-08-24, 15 LT	DIA-CFH	None	MIAWARA, RALMO
5	2023-08-29, 23 LT	PCFH, DIA-CFH	None	MIAWARA, RALMO
6	2023-09-04, 15 LT	DIA-CFH	None	MIAWARA, RALMO
7	2023-09-07, 00 LT	PCFH, DIA-CFH	None	MIAWARA, RALMO
8	2024-04-29, 22 LT	PCFH, DIA-CFH	None	MIAWARA, RALMO
9	2024-05-01, 22 LT	PCFH, DIA-CFH	None	MIAWARA, RALMO
10	2024-05-03, 12 LT	DIA-CFH	None	MIAWARA
11	2024-05-06, 22 LT	PCFH, DIA-CFH	None	MIAWARA
12	2024-06-17, 22 LT	PCFH, DIA-CFH	None	MIAWARA
13	2024-06-18, 22 LT	PCFH, DIA-CFH	ALBATROSS	MIAWARA
14	2024-06-19, 15 LT	DIA-CFH	None	MIAWARA
15	2024-06-26, 22 LT	PCFH, DIA-CFH	None	MIAWARA, RALMO
16	2024-09-12, 20 LT	PCFH	DIA-CFH, CFH	MIAWARA
17	2024-09-19, 03 LT	PCFH, CFH	ALBATROSS	MIAWARA, RALMO
18	2025-03-24, 22 LT	DIA-CFH, CFH	None	MIAWARA, RALMO
19	2025-03-27, 23 LT	PCFH, DIA-CFH	ALBATROSS, CFH	MIAWARA, RALMO
20	2025-07-01, 00 LT	PCFH, CFH	ALBATROSS, CFH	MIAWARA, RALMO, CRYOWARA
21	2025-07-03, 00 LT	PCFH, CFH	DIA-CFH, CFH	MIAWARA, RALMO
22	2025-08-18, 23 LT	PCFH, CFH	DIA-CFH, CFH	MIAWARA, RALMO
23	2025-08-22, 08 LT	DIA-CFH, CFH	DIA-CFH	MIAWARA, RALMO
24	2025-09-02, 15 LT	DIA-CFH, CFH	None	MIAWARA, RALMO
25	2025-09-04, 01 LT	PCFH, DIA-CFH	None	MIAWARA
26	2025-09-05, 11 LT	DIA-CFH, CFH	None	MIAWARA, RALMO
27	2025-09-18, 23 LT	DIA-CFH, CFH	None	MIAWARA, RALMO
28	2025-10-21, 15 LT	DIA-CFH	None	MIAWARA, RALMO
29	2025-12-12, 00 LT	PCFH, CFH	None	MIAWARA
30	2026-05-01, 00 LT	PCFH, CFH	ALBATROSS, CFH	MIAWARA, RALMO
31	2026-06-25, 23 LT	PCFH, DIA-CFH	DIA-CFH, CFH	MIAWARA, RALMO
32	2026-08-19, 22 LT	PCFH, DIA-CFH	None	MIAWARA, RALMO

https://doi.org/10.5194/egusphere-2026-7088
Preprint. Discussion started: 23 November 2026
© Author(s) 2026. CC BY 4.0 License.

Appendix B: Supplementary Figures

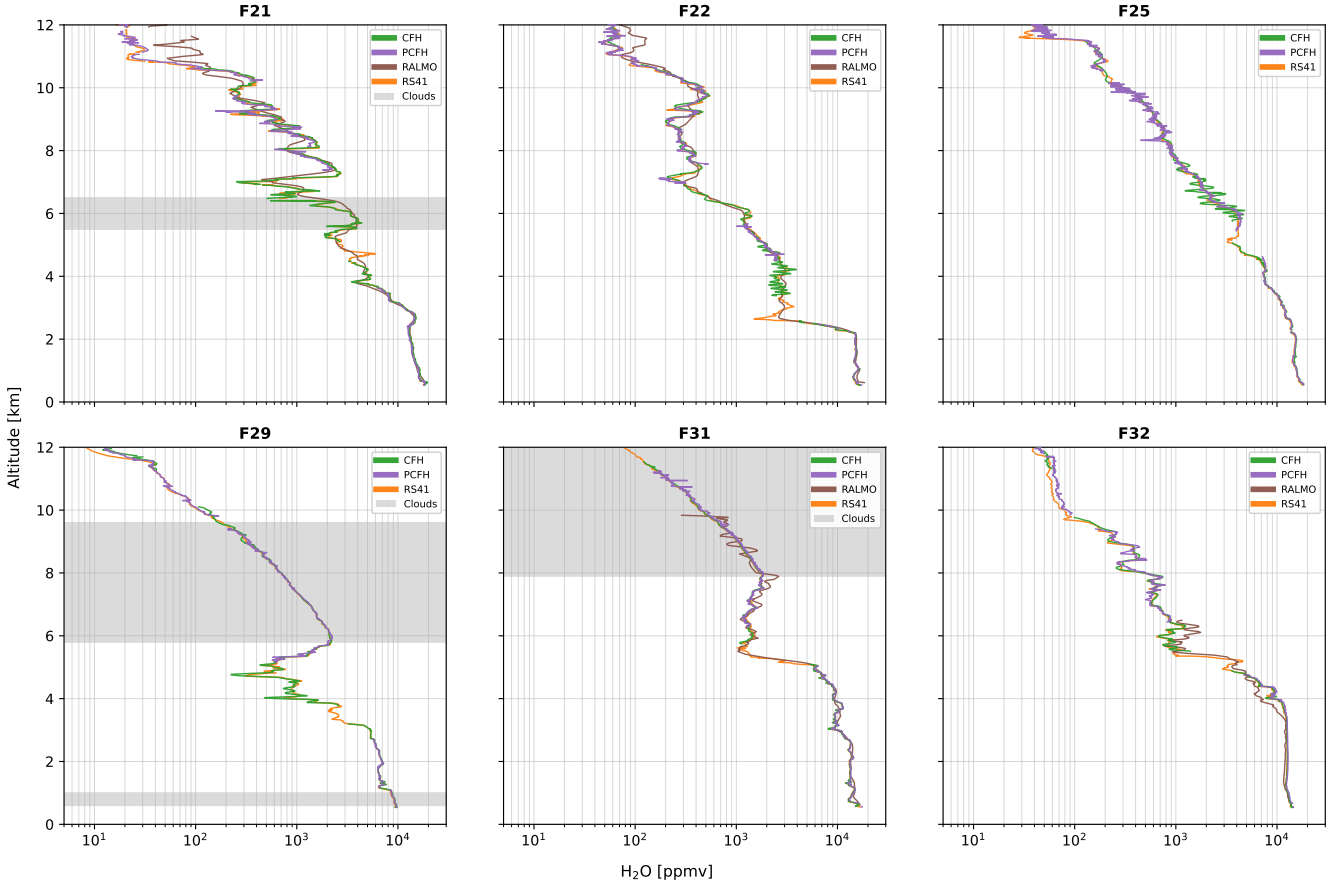

Figure B1. Vertical profiles of H_2O mixing ratio in the troposphere (0–12 km) for the six flights contributing to the PCFH and RALMO comparisons on which ALBATROSS was not deployed: flights 21, 22, 25, 29, 31, 32, all ascent.

https://doi.org/10.5194/egusphere-2026-7088
Preprint. Discussion started: 23 November 2026
© Author(s) 2026. CC BY 4.0 License.

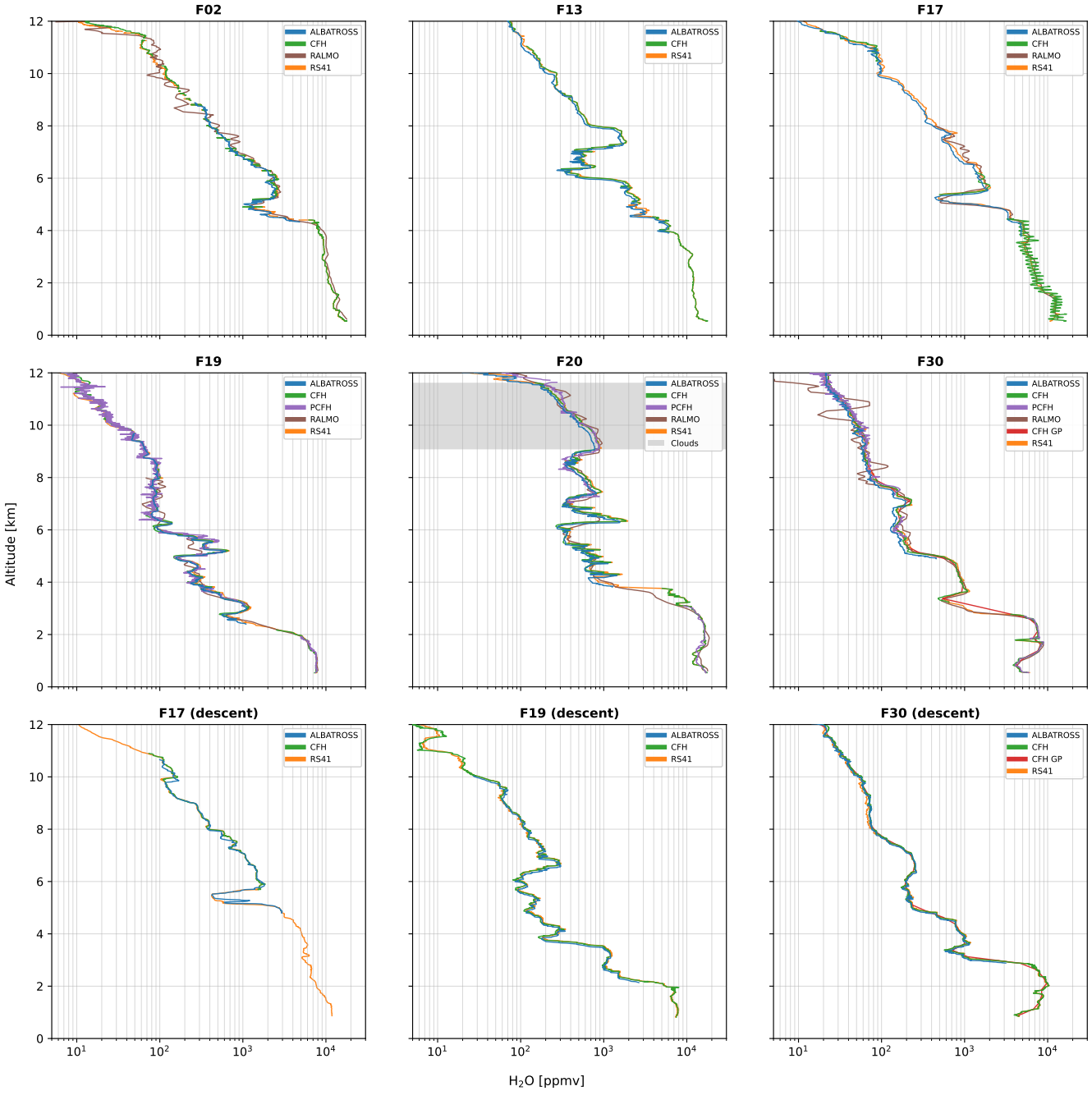

Figure B2. Vertical profiles of H_2O mixing ratio in the troposphere (0–12 km) for the six flights contributing to the ALBATROSS comparison (flights 2, 13, 17, 19, 20 and 30), followed by the three flights whose descent also contributes (flights 17, 19 and 30). Gray shaded areas indicate cloud layers. For flight 30, the CFH profile processed by the Golden-Point method down-sampled to 250 m resolution (CFH GP, red trace) is also shown.

https://doi.org/10.5194/egusphere-2026-7088
Preprint. Discussion started: 23 November 2026
© Author(s) 2026. CC BY 4.0 License.

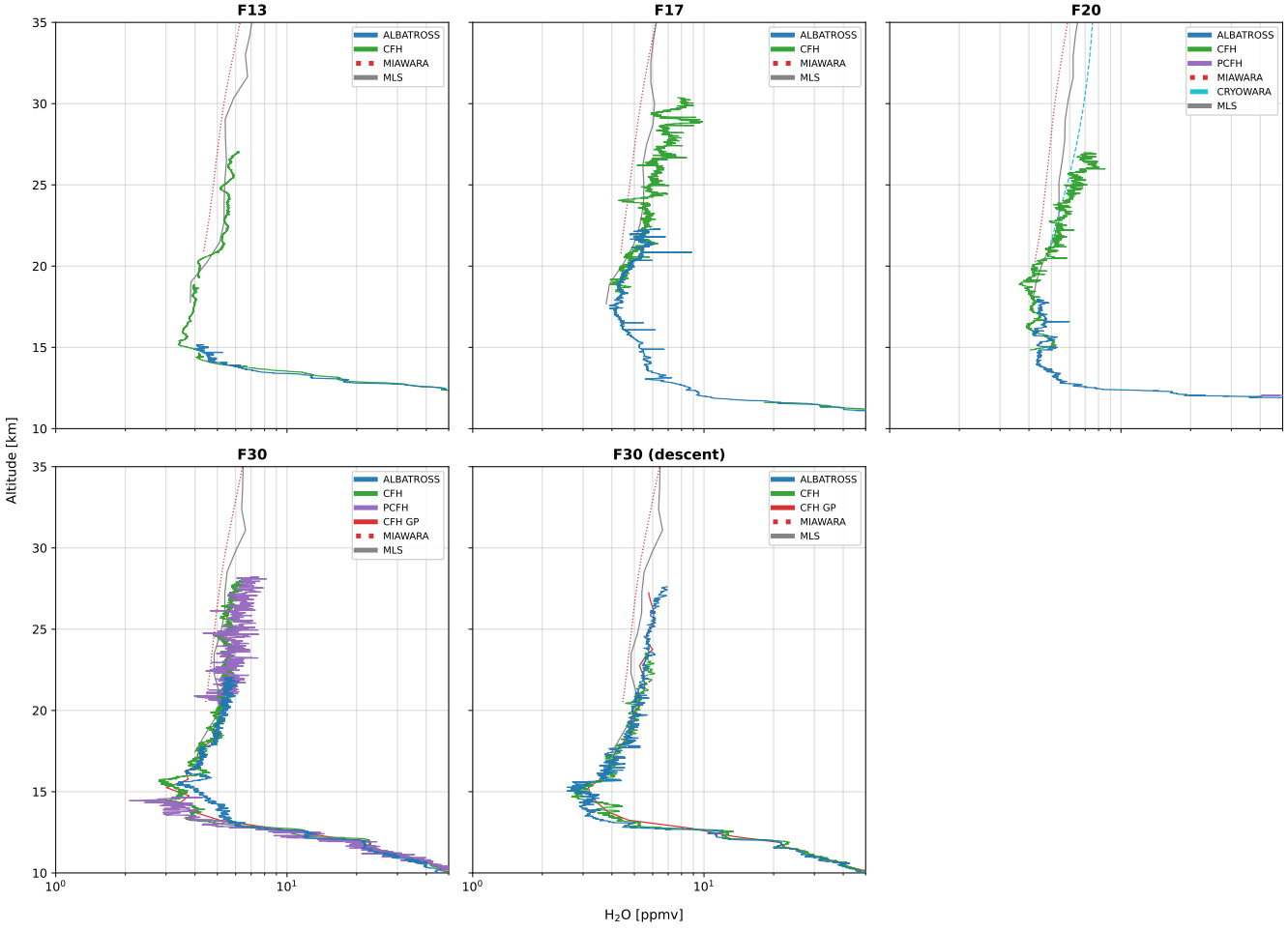

Figure B3. UTLS vertical profiles (10–35 km) for the four flights contributing to the ALBATROSS stratospheric comparison (13, 17, 20 and 30), with the descent of flight 30 shown as a separate panel. For flight 20, the CRYOWARA retrieval (cyan, dashed) is also available, and for flight 30 the Golden-Point CFH down-sampled to 500 m resolution above 12 km and 250 m below (red). MIAWARA and CRYOWARA are shown only above 20 km.

https://doi.org/10.5194/egusphere-2026-7088
Preprint. Discussion started: 23 November 2026
© Author(s) 2026. CC BY 4.0 License.

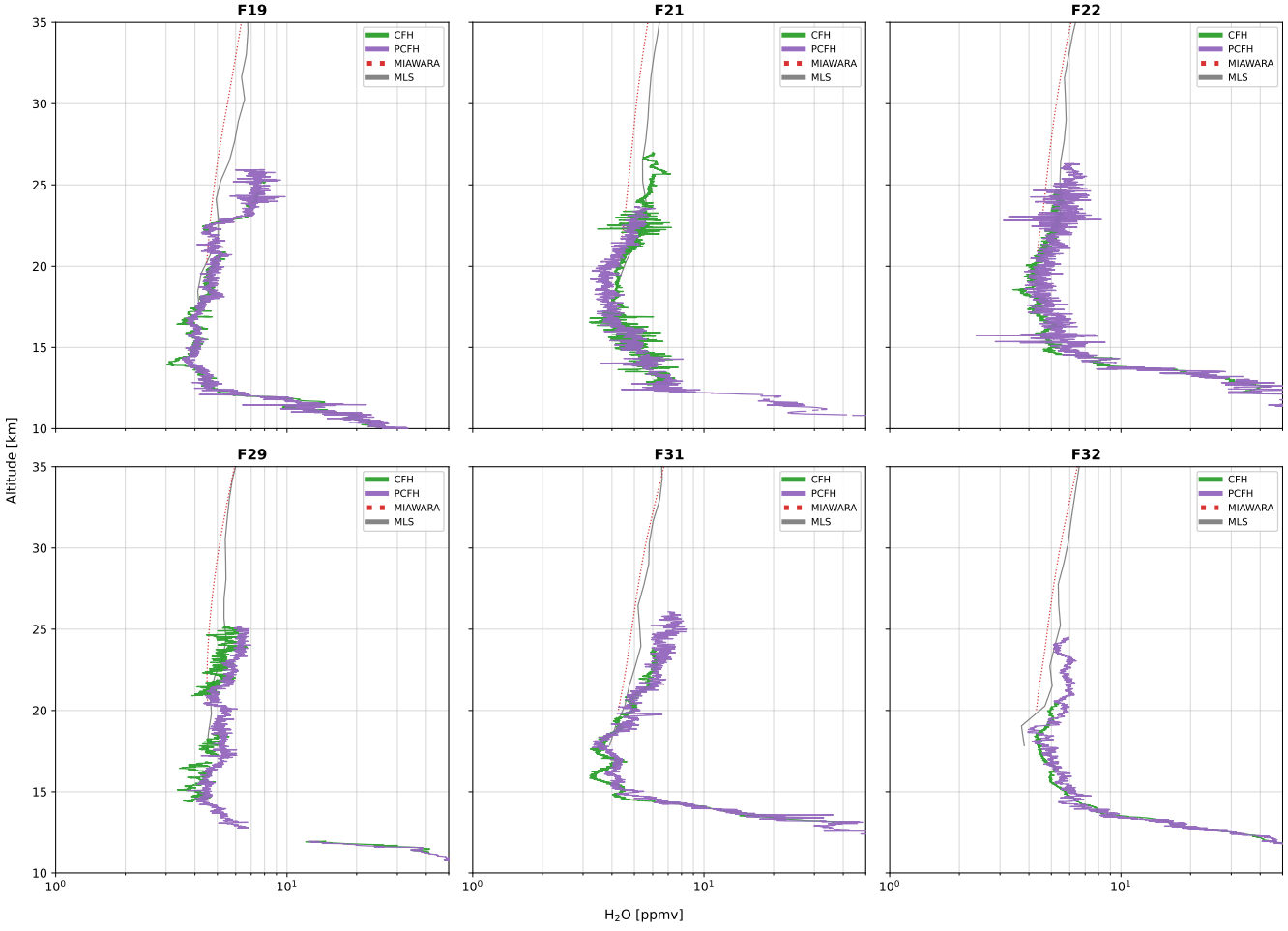

Figure B4. UTLS vertical profiles (10–35 km), for the six flights contributing to the PCFH stratospheric comparison, where ALBATROSS is absent: flights 19, 21, 22, 29, 31 and 32, all ascent.

https://doi.org/10.5194/egusphere-2026-7088
Preprint. Discussion started: 23 November 2026
© Author(s) 2026. CC BY 4.0 License.

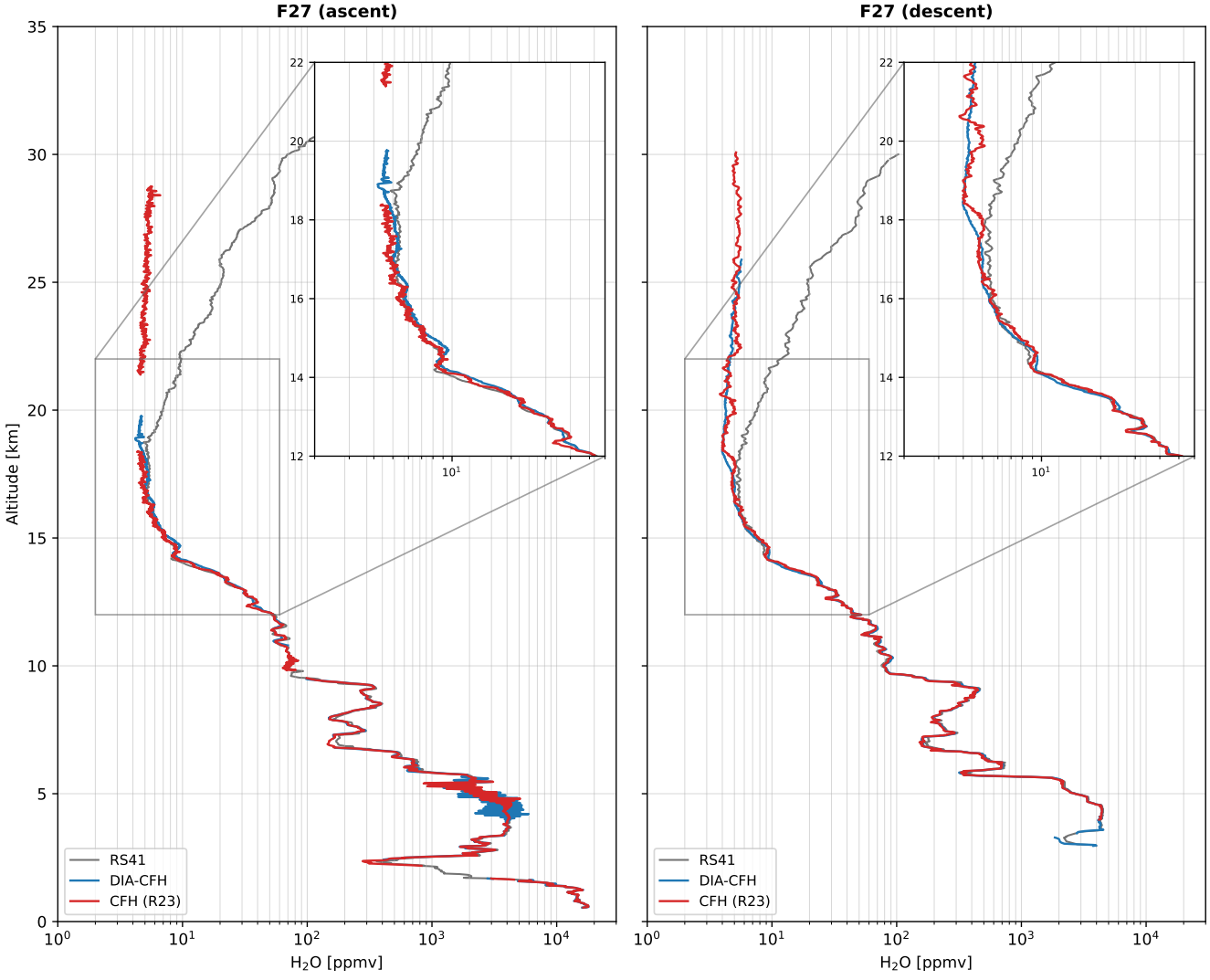

Figure B5. Vertical profiles of H_2O mixing ratio from flight 27, comparing the CFH operated with the conventional R23 refrigerant (red) against the dry-ice/alcohol configuration (DIA-CFH, blue), on the ascent (left) and the descent (right). The RS41 profile from the same balloon is shown in gray.

https://doi.org/10.5194/egusphere-2026-7088
Preprint. Discussion started: 23 November 2026
© Author(s) 2026. CC BY 4.0 License.

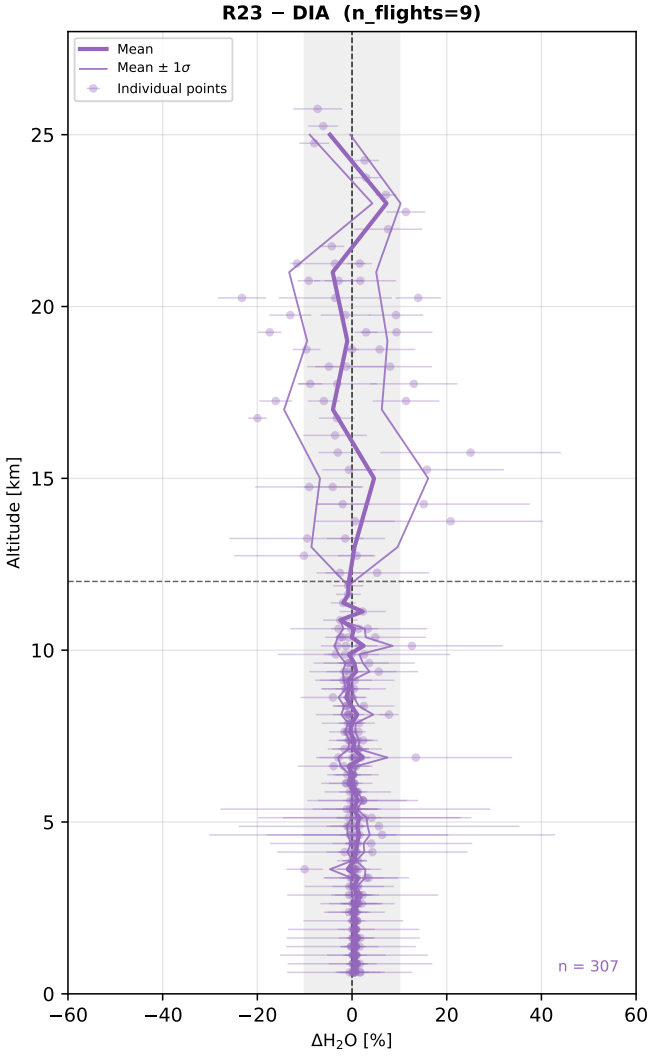

Figure B6. Statistical comparison: relative difference in H_2O mixing ratio between the two CFH cooling configurations, R23 with respect to DIA, over the full sounding column (0–28 km), from the nine flights (16, 18, 21, 22, 23, 24, 26, 27, 31) carrying both instruments on the same payload. Each point is one flight's mean relative difference in one altitude bin, with the horizontal bar giving the standard deviation of the differences within that bin; the solid line is the mean across all flights and the thin lines the ± 1 standard deviation about it. The gray band marks the $\pm 10\%$ agreement level, and the number of contributing flights and comparison points is given in the panel.

https://doi.org/10.5194/egusphere-2026-7088
Preprint. Discussion started: 23 November 2026
© Author(s) 2026. CC BY 4.0 License.

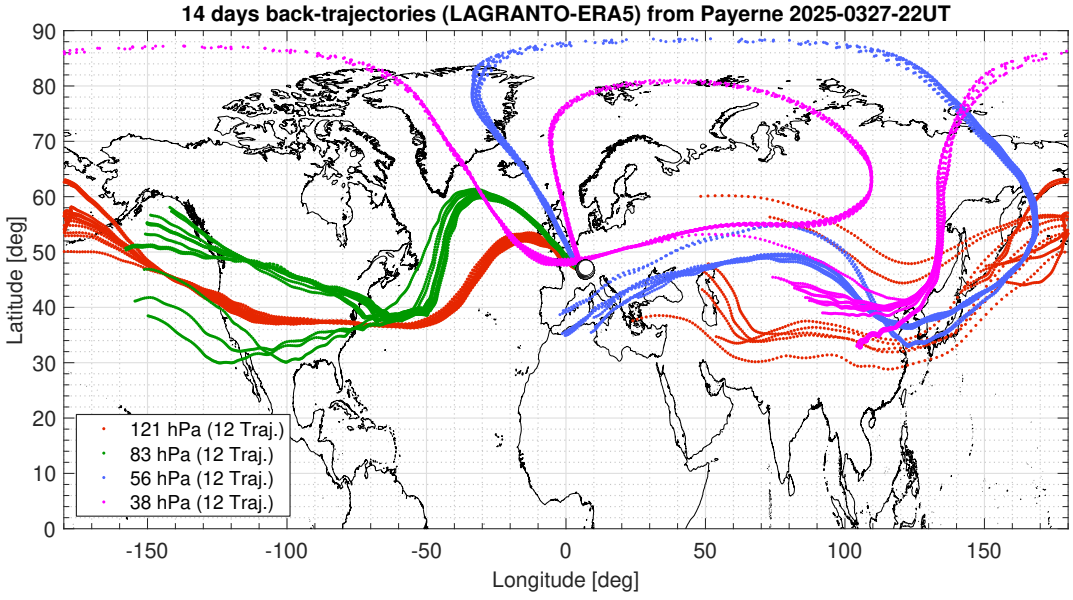

Figure B7. ERA5-LAGRANTO (Sprenger and Wernli, 2015) swarms of 12 two-week backtrajectories starting from various UTLS pressure levels above Payerne on flight 19.

Data availability. The data will be uploaded to a public data repository (DOI will be added).

Author contributions. AF was responsible for the development of the new radiometer CRYOWARA with the support of ABe, AM, and GS. YP was responsible for the preparation and deployment of CFH variants and data analysis of CFH, with support from VA, ABr and TP. SBru was responsible for the final development, testing, preparation, deployment, and data analysis of the ALBATROSS spectrometer, with support from AW and BT. FGW was responsible for the preparation, deployment, and data analysis of PCFH with support from YP, SBro, VA, and ABr. GM was responsible for the data analysis of RALMO with support from RM. GR contributed to instrument preparation, flight planning, design and data analysis, and coordinated balloon operations at Payerne, including airspace coordination with Skyguide and balloon launches. GS, AM, LE, FGW and AH provided scientific coordination and institutional support. This manuscript was written by AF with support and input from YP, SBru, FGW, GM, and edits from BT, TP and GS. All co-authors have reviewed and validated the manuscript. The project was supervised by GS.

Competing interests. The contact author has declared that none of the authors has any competing interests.

https://doi.org/10.5194/egusphere-2026-7088
Preprint. Discussion started: 23 November 2026
© Author(s) 2026. CC BY 4.0 License.



Acknowledgements. We thank Jean-Claude Aubort (MeteoSwiss), Alain Rey (MeteoSwiss) and Thomas Brossi (mylab) for valuable additional assistance during flight activities. The GRUAN and NDACC communities are acknowledged for fruitful discussions on payload preparation and handling of telemetry issues. The authors further acknowledge the operational support of MeteoSwiss and the institutional support provided by ETH Zurich, Empa, MeteoSwiss, and the University of Bern, in which AB, AF, AM, GS, and YP are also members of the Oeschger Centre for Climate Change Research.

Financial Support. This work was supported by the "Swiss H2O Hub for high-quality water vapor measurements from ground to space" project financed by GCOS Switzerland (MeteoSwiss, 2026).

The PCFH development has been supported by the environmental technology promotion of the Swiss Federal Office for the Environment (FOEN) under project ID UTF 705.25.22: PCFH Peltier Cooled Frost Point Hygrometer: vom Prototyp zum Seriengerät (last access 11 Aug 2026).

https://doi.org/10.5194/egusphere-2026-7088
Preprint. Discussion started: 23 November 2026
© Author(s) 2026. CC BY 4.0 License.

References

Akmaev, R., Fomichev, V., and Zhu, X.: Impact of middle-atmospheric composition changes on greenhouse cooling in the upper atmosphere, Journal of Atmospheric and Solar-Terrestrial Physics, 68, 1879–1889, https://doi.org/10.1016/j.jastp.2006.03.008, 2006.

Andrews, D., Holton, J., and Leovy, C.: Middle Atmosphere Dynamics, International Geophysics (Vol. 40), Academic Press, ISBN 978-0-12-058575-5, 1987.

Barrera-Verdejo, M., Crewell, S., Löhnert, U., Orlandi, E., and Di Girolamo, P.: Ground-based lidar and microwave radiometry synergy for high vertical resolution absolute humidity profiling, Atmospheric Measurement Techniques, 9, 4013–4028, https://doi.org/10.5194/amt-9-4013-2016, 2016.

Bell, A. and Murk, A.: Monitoring of Middle Atmospheric Water Vapour, Tech. rep., Swiss GCOS Office, https://www.meteoswiss.admin.ch/dam/jcr:94899c15-57ba-4969-a56a-11781d0de260/Final-report-MIAWARA-GCOS.pdf, doi:10.48350/183553, accessed: 2026-08-03, 2023.

Bell, A., Murk, A., and Stober, G.: Radiative impact of increased middle atmospheric water vapour in the aftermath of the Hunga 2022 volcanic eruption at two locations in the Northern Hemisphere, EGUsphere, 2025, 1–22, https://doi.org/10.5194/egusphere-2025-1396, 2025a.

Bell, A., Sauvageat, E., Stober, G., Hocke, K., and Murk, A.: Developments on a 22 GHz microwave radiometer and reprocessing of 13-year time series for water vapour studies, Atmospheric Measurement Techniques, 18, 555–567, https://doi.org/10.5194/amt-18-555-2025, 2025b.

Bodeker, G. E., Bojinski, S., Cimini, D., Dirksen, R. J., Haeffelin, M., Hannigan, J. W., Hurst, D. F., Leblanc, T., Madonna, F., Maturilli, M., Mikalsen, A. C., Philipona, R., Reale, T., Seidel, D. J., Tan, D. G. H., Thorne, P. W., Vömel, H., and Wang, J.: Reference Upper-Air Observations for Climate: From Concept to Reality, Bulletin of the American Meteorological Society, 97, 123–135, https://doi.org/10.1175/BAMS-D-14-00072.1, 2016.

Brasseur, G. P. and Solomon, S.: Aeronomy of the Middle Atmosphere: Chemistry and Physics of the Stratosphere and Mesosphere, vol. 32, Springer, Dordrecht, 3 edn., https://doi.org/10.1007/1-4020-3824-0, 2005.

Brunamonti, S., Jorge, T., Oelsner, P., Hanumanthu, S., Singh, B. B., Ravi Kumar, K., Sonbawne, S., Meier, S., Singh, D., Wienhold, F. G., Ping Luo, B., Boettcher, M., Poltera, Y., Jauhiainen, H., Kayastha, R., Karmacharya, J., DIrksen, R., Naja, M., Rex, M., Fadnavis, S., and Peter, T.: Balloon-borne measurements of temperature, water vapor, ozone and aerosol backscatter on the southern slopes of the Himalayas during StratoClim 2016-2017, Atmospheric Chemistry and Physics, 18, 15 937–15 957, https://doi.org/10.5194/acp-18-15937-2018, 2018.

Brunamonti, S., Martucci, G., Romanens, G., Poltera, Y., Wienhold, F. G., Hervo, M., Haefele, A., and Navas-Guzmán, F.: Validation of aerosol backscatter profiles from Raman lidar and ceilometer using balloon-borne measurements, Atmos. Chem. Phys., 21, 2267–2285, https://doi.org/10.5194/acp-21-2267-2021, 2021.

Brunamonti, S., Graf, M., Bühlmann, T., Pascale, C., Ilak, I., Emmenegger, L., and Tuzson, B.: SI-traceable validation of a laser spectrometer for balloon-borne measurements of water vapor in the upper atmosphere, Atmospheric Measurement Techniques, 16, 4391–4408, https://doi.org/10.5194/amt-16-4391-2023, 2023.

Brunamonti, S., Saathoff, H., Hertzog, A., Diskin, G., Fujiwara, M., Rosenlof, K., Möhler, O., Tuzson, B., Emmenegger, L., Amarouche, N., Durry, G., Frérot, F., Samake, J.-C., Cenac, C., Lopez, J., Monnier, P., and Ghysels, M.: The AquaVIT-4 intercomparison of atmospheric hygrometers, Atmospheric Measurement Techniques, 18, 5321–5348, https://doi.org/10.5194/amt-18-5321-2025, 2025.

https://doi.org/10.5194/egusphere-2026-7088
Preprint. Discussion started: 23 November 2026
© Author(s) 2026. CC BY 4.0 License.

Brunamonti, S., Poltera, Y., Romanens, G., Weitnauer, A., Scheidegger, P., Filinis, A., Bell, A., Martucci, G., Wienhold, F. G., Peter, T., Oelsner, P., Dirksen, R., Haefele, A., Emmenegger, L., Stober, G., and Tuzson, B.: Accurate and high-resolution measurements of UTLS water vapor by balloon-borne laser absorption spectroscopy, EGUsphere, 2026, 1–27, https://doi.org/10.5194/egusphere-2026-4762, 2026.

Chouza, F., Leblanc, T., Brewer, M., Wang, P., Martucci, G., Haefele, A., Vérèmes, H., Duflot, V., Payen, G., and Keckhut, P.: The impact of aerosol fluorescence on long-term water vapor monitoring by Raman lidar and evaluation of a potential correction method, Atmospheric Measurement Techniques, 15, 4241–4256, https://doi.org/10.5194/amt-15-4241-2022, 2022.

Crezee, B., Martucci, G., Leuenberger, D., Merker, C., Haefele, A., and Arpagaus, M.: Assimilation of Raman lidar profiles in an operational, convective-scale numerical weather prediction model, Quarterly Journal of the Royal Meteorological Society, 151, e5023, https://doi.org/10.1002/qj.5023, 2025.

Deuber, B., Kampfer, N., and Feist, D. G.: A new 22-GHz radiometer for middle atmospheric water vapor profile measurements, IEEE Transactions on Geoscience and Remote Sensing, 42, 974–984, https://doi.org/10.1109/TGRS.2004.825581, 2004.

Díaz-Zurita, A., Brunamonti, S., Haefele, A., Collaud Coen, M., Martucci, G., Brem, B. T., Gysel-Beer, M., Lyamani, H., Titos, G., Pérez-Ramírez, D., Hüglin, C., Alados-Arboledas, L., Keller, A., Wienhold, F. G., Hervo, M., and Navas-Guzmán, F.: Characterisation of hygroscopic aerosol processes using remote sensing and in situ techniques at the MeteoSwiss Payerne station, EGUsphere, 2026, 1–44, https://doi.org/10.5194/egusphere-2026-4361, 2026.

Dinoev, T., Simeonov, V., Arshinov, Y., Bobrovnikov, S., Ristori, P., Calpini, B., Parlange, M., and van den Bergh, H.: Raman lidar for meteorological observations, RALMO–Part 1: Instrument description, Atmospheric Measurement Techniques, 6, 1329–1346, https://doi.org/10.5194/amt-6-1329-2013, 2013.

Dirksen, R.: Report on tests in Lindenberg, in: 12th GRUAN Implementation and Coordination Meeting, Virtual, 16 to 20 November 2020, GCOS-237 report, https://www.gruan.org/gruan/editor/documents/meetings/icm-12/pres/pres_304_Dirksen_CFH-LIN.pdf, accessed: 2026-05-22, 2020.

Dirksen, R. et al.: Report of WMO's 2022 Upper-Air Instrument Intercomparison Campaign, IOM-143, World Meteorological Organization, https://library.wmo.int/idurl/4/68808, accessed: 2026-05-22, 2024.

Dirksen, R. J., Sommer, M., Immler, F. J., Hurst, D. F., Kivi, R., and Vömel, H.: Reference quality upper-air measurements: GRUAN data processing for the Vaisala RS92 radiosonde, Atmospheric Measurement Techniques, 7, 4463–4490, https://doi.org/10.5194/amt-7-4463-2014, 2014.

Droniq GmbH: Ping20Si - Mini Mode-S Transponder für den Drohnenbetrieb, https://droniq.de/produkte/ping20si/, accessed: 2026-05-26, 2024.

EC: Commission Implementing Regulation (EU) No 923/2012 of 26 September 2012, Official Journal of the European Union, 281, 1–66, https://eur-lex.europa.eu/legal-content/EN/TXT/PDF/?uri=CELEX:32012R0923&from=EN, accessed: 2026-01-26, 2012.

Fahey, D. W., Gao, R.-S., Möhler, O., Saathoff, H., Schiller, C., Ebert, V., Krämer, M., Peter, T., Amarouche, N., Avallone, L. M., Bauer, R., Bozóki, Z., Christensen, L. E., Davis, S. M., Durry, G., Dyroff, C., Herman, R. L., Hunsmann, S., Khaykin, S. M., Mackrodt, P., Meyer, J., Smith, J. B., Spelten, N., Troy, R. F., Vömel, H., Wagner, S., and Wienhold, F. G.: The AquaVIT-1 intercomparison of atmospheric water vapor measurement techniques, Atmospheric Measurement Techniques, 7, 3177–3213, https://doi.org/10.5194/amt-7-3177-2014, 2014.

Farhani, G., Martucci, G., Roberts, T., Haefele, A., and Sica, R. J.: A Bayesian neural network approach for tropospheric temperature retrievals from a lidar instrument, International Journal of Remote Sensing, 44, 1611–1627, https://doi.org/10.1080/01431161.2023.2187723, 2023.

https://doi.org/10.5194/egusphere-2026-7088
Preprint. Discussion started: 23 November 2026
© Author(s) 2026. CC BY 4.0 License.



Filinis, A., Bell, A., Murk, A., and Stober, G.: Development of a new cryogenically cooled water vapor radiometer for the 22 GHz line – quasi-optical design and preliminary laboratory receiver tests, Atmospheric Measurement Techniques, 19, 1783–1799, https://doi.org/10.5194/amt-19-1783-2026, 2026.

Gerding, M., Höffner, J., Hoffmann, P., Kopp, M., and Lübken, F.-J.: Noctilucent cloud variability and mean parameters from 15 years of lidar observations at a mid-latitude site (54°N, 12°E), Journal of Geophysical Research: Atmospheres, 118, 317–328, https://doi.org/10.1029/2012JD018319, 2013.

Graf, M., Emmenegger, and Tuzson, B.: Compact, circular, and optically stable multipass cell for mobile laser absorption spectroscopy, Optics Letters, 43, 2434–2437, https://doi.org/10.1364/OL.43.002434, 2018.

Graf, M., Scheidegger, P., Kupferschmid, A., Looser, H., Peter, T., Dirksen, R., Emmenegger, L., and Tuzson, B.: Compact and lightweight mid-infrared laser spectrometer for balloon-borne water vapor measurements in the UTLS, Atmospheric Measurement Techniques, 14, 1365–1383, https://doi.org/10.5194/amt-14-1365-2021, 2021.

Gustincic, J.: A quasi-optical receiver design, in: 1977 IEEE MTT-S International Microwave Symposium Digest, pp. 99–102, IEEE, https://doi.org/10.1109/MWSYM.1977.1124373, 1977.

Haefele, A., De Wachter, E., Hocke, K., Kämpfer, N., Nedoluha, G. E., Gomez, R. M., Eriksson, P., Forkman, P., Lambert, A., and Schwartz, M. J.: Validation of ground-based microwave radiometers at 22 GHz for stratospheric and mesospheric water vapor, Journal of Geophysical Research: Atmospheres, 114, https://doi.org/10.1029/2009JD011997, 2009.

Hall, E. G., Jordan, A. F., Hurst, D. F., Oltmans, S. J., Vömel, H., Kühnreich, B., and Ebert, V.: Advancements, measurement uncertainties, and recent comparisons of the NOAA frost point hygrometer, Atmospheric Measurement Techniques, 9, 4295–4310, https://doi.org/10.5194/amt-9-4295-2016, 2016.

Hallgren, K. and Hartogh, P.: First Detection of Tidal Behaviour in Polar Mesospheric Water Vapour by Ground Based Microwave Spectroscopy, Atmospheric Chemistry and Physics, 12, 3753–3759, https://doi.org/10.5194/acp-12-3753-2012, 2012.

Hallgren, K., Hartogh, P., and Jarchow, C.: A New, High-Performance, Heterodyne Spectrometer for Ground-Based Remote Sensing of Mesospheric Water Vapour, in: Advances in Geosciences, vol. 19, pp. 569–578, World Scientific, https://doi.org/10.1142/9789812838162_0042, 2010.

Hardy, B.: ITS-90 Formulations for Vapor Pressure, Frostpoint Temperature, Dewpoint Temperature, and Enhancement Factors in the Range -100 to +100 °C, in: Proceedings of the Third International Symposium on Humidity and Moisture, vol. 1, pp. 214–222, Teddington, London, England, https://www.thunderscientific.com/wp-content/uploads/2022/12/its90formulas.pdf, accessed 2026-05-22, 1998.

Hartogh, P. and Jarchow, C.: Ground-based detection of middle atmospheric water vapor, in: Global Process Monitoring and Remote Sensing of the Ocean and Sea Ice, edited by Deering, D. W. and Gudmandsen, P., vol. 2586, pp. 188 – 195, International Society for Optics and Photonics, SPIE, https://doi.org/10.1117/12.228622, 1995.

Hauchecorne, A., Keckhut, P., and Chanin, M.-L.: Dynamics and transport in the middle atmosphere using remote sensing techniques from ground and space, in: Infrasound monitoring for atmospheric studies, pp. 665–683, Springer, Dordrecht, https://doi.org/10.1007/978-1-4020-9508-5_22, 2009.

Hervig, M., McHugh, M., and Summers, M. E.: Water vapor enhancement in the polar summer mesosphere and its relationship to polar mesospheric clouds, Geophysical Research Letters, 30, https://doi.org/10.1029/2003GL018089, 2003.

Hervig, M. E., Siskind, D. E., Bailey, S. M., and Russell, J. M.: The influence of PMCs on water vapor and drivers behind PMC variability from SOFIE observations, Journal of Atmospheric and Solar-Terrestrial Physics, 132, 124–134, https://doi.org/10.1016/j.jastp.2015.07.010, 2015.

https://doi.org/10.5194/egusphere-2026-7088
Preprint. Discussion started: 23 November 2026
© Author(s) 2026. CC BY 4.0 License.

Hicks-Jalali, S., Sica, R. J., Martucci, G., Maillard Barras, E., Voirin, J., and Haefele, A.: A Raman lidar tropospheric water vapour climatology and height-resolved trend analysis over Payerne, Switzerland, Atmospheric Chemistry and Physics, 20, 9619–9640, https://doi.org/10.5194/acp-20-9619-2020, 2020.

Immler, F. J., Dykema, J., Gardiner, T., Whiteman, D. N., Thorne, P. W., and Vömel, H.: Reference Quality Upper-Air Measurements: guidance for developing GRUAN data products, Atmospheric Measurement Techniques, 3, 1217–1231, https://doi.org/10.5194/amt-3-1217-2010, 2010.

Janssen, M. A.: Atmospheric Remote Sensing by Microwave Radiometry, Wiley, New York, NY, ISBN 0471628913, 1993.

Jayaweera, V., Sica, R. J., Martucci, G., and Haefele, A.: Solar background radiation temperature calibration of a pure rotational Raman lidar, Atmospheric Measurement Techniques, 18, 1461–1469, https://doi.org/10.5194/amt-18-1461-2025, 2025.

Jensen, M. P., Holdridge, D. J., Survo, P., Lehtinen, R., Baxter, S., Toto, T., and Johnson, K. L.: Comparison of Vaisala Radiosondes RS41 and RS92 at the ARM Southern Great Plains Site, Atmospheric Measurement Techniques, 9, 3115–3129, https://doi.org/10.5194/amt-9-3115-2016, 2016.

Jet Propulsion Laboratory: Version 5.0x Level 2 and 3 Data Quality and Description Document, Tech. rep., Jet Propulsion Laboratory, California Institute of Technology, https://mls.jpl.nasa.gov/data/v5-0_data_quality_document.pdf, aura Microwave Limb Sounder data quality document, published 9 June 2020, accessed 2026-04-17, 2020.

Jorge, T.: Developments in balloon-borne water vapour measurements with frost point hygrometers, Doctoral Thesis (ETH Zurich), https://doi.org/10.3929/ethz-b-000411391, 2019.

Jorge, T., Brunamonti, S., Poltera, Y., Wienhold, F. G., Luo, B. P., Oelsner, P., Hanumanthu, S., Singh, B. B., Körner, S., Dirksen, R., Naja, M., Fadnavis, S., and Peter, T.: Understanding balloon-borne frost point hygrometer measurements after contamination by mixed-phase clouds, Atmospheric Measurement Techniques, 14, 239–268, https://doi.org/10.5194/amt-14-239-2021, 2021.

Kandel, R. and Viollier, M.: Observation of the Earth's radiation budget from space, Comptes Rendus Géoscience, 342, 286–300, https://doi.org/10.1016/j.crte.2010.01.005, 2010.

Lambert, A., Read, W. G., Livesey, N. J., Santee, M. L., Manney, G. L., Froidevaux, L., Wu, D. L., Schwartz, M. J., Pumphrey, H. C., Jimenez, C., Nedoluha, G. E., Cofield, R. E., Cuddy, D. T., Daffer, W. H., Drouin, B. J., Fuller, R. A., Jarnot, R. F., Knosp, B. W., Pickett, H. M., Perun, V. S., Snyder, W. V., Stek, P. C., Thurstans, R. P., Wagner, P. A., Waters, J. W., Jucks, K. W., Toon, G. C., Stachnik, R. A., Bernath, P. F., Boone, C. D., Walker, K. A., Urban, J., Murtagh, D., Elkins, J. W., and Atlas, E.: Validation of the Aura Microwave Limb Sounder middle atmosphere water vapor and nitrous oxide measurements, Journal of Geophysical Research: Atmospheres, 112, D24S36, https://doi.org/10.1029/2007JD008724, 2007.

Leuenberger, D., Haefele, A., Omanovic, N., Fengler, M., Martucci, G., Calpini, B., Fuhrer, O., and Rossa, A.: Improving High-Impact Numerical Weather Prediction with Lidar and Drone Observations, Bulletin of the American Meteorological Society, 101, E1036 – E1051, https://doi.org/10.1175/BAMS-D-19-0119.1, 2020.

Livesey, N. J., Read, W. G., Froidevaux, L., Lambert, A., Santee, M. L., Schwartz, M. J., Millán, L. F., Jarnot, R. F., Wagner, P. A., Hurst, D. F., Walker, K. A., Sheese, P. E., and Nedoluha, G. E.: Investigation and amelioration of long-term instrumental drifts in water vapor and nitrous oxide measurements from the Aura Microwave Limb Sounder (MLS) and their implications for studies of variability and trends, Atmospheric Chemistry and Physics, 21, 15 409–15 430, https://doi.org/10.5194/acp-21-15409-2021, 2021.

Martucci, G., Navas-Guzmán, F., Renaud, L., Romanens, G., Gamage, S. M., Hervo, M., Jeannet, P., and Haefele, A.: Validation of pure rotational Raman temperature data from the Raman Lidar for Meteorological Observations (RALMO) at Payerne, Atmospheric Measurement Techniques, 14, 1333–1353, https://doi.org/10.5194/amt-14-1333-2021, 2021.

https://doi.org/10.5194/egusphere-2026-7088
Preprint. Discussion started: 23 November 2026
© Author(s) 2026. CC BY 4.0 License.

Masoom, A., Kazadzis, S., Modini, R. L., Gysel-Beer, M., Gröbner, J., Coen, M. C., Navas-Guzman, F., Kouremeti, N., Brem, B. T., Nowak, N. K., Martucci, G., and Hervo, M.: Long range transport of Canadian wildfire smoke to Europe in 2023: aerosol properties and spectral features of smoke particles, Atmospheric Chemistry and Physics, 26, 10 801–10 834, https://doi.org/10.5194/acp-26-10801-2026, 2026.

Mastenbrook, H. J. and Oltmans, S. J.: Stratospheric Water Vapor Variability for Washington, DC/Boulder, CO: 1964–82, Journal of the Atmospheric Sciences, 40, 2157–2165, https://doi.org/10.1175/1520-0469(1983)040<2157:SWVVFW>2.0.CO;2, 1983.

MeteoSwiss: GAW-CH and GCOS-CH supported activities, Web page, https://www.meteoswiss.admin.ch/about-us/research-and-cooperation/programmes-gaw-ch-and-gcos-ch/gaw-ch-and-gcos-ch-supported-activities.html, accessed: 2026-08-26, 2026.

Mevi, G., Muscari, G., Bertagnolio, P. P., Fiorucci, I., and Pace, G.: VESPA-22: a ground-based microwave spectrometer for long-term measurements of polar stratospheric water vapor, Atmospheric Measurement Techniques, 11, 1099–1117, https://doi.org/10.5194/amt-11-1099-2018, 2018.

Millán, L., Santee, M. L., Lambert, A., Livesey, N. J., Werner, F., Schwartz, M. J., Pumphrey, H. C., Manney, G. L., Wang, Y., Su, H., Wu, L., Read, W. G., and Froidevaux, L.: The Hunga Tonga–Hunga Ha'apai Hydration of the Stratosphere, Geophysical Research Letters, 49, e2022GL099 381, https://doi.org/10.1029/2022GL099381, 2022.

MLS Science Team: Aura MLS Data: Duty Cycling of the 190-GHz Observations, Jet Propulsion Laboratory, Aura MLS data web page, https://mls.jpl.nasa.gov/eos-aura-mls/data.php, accessed 2026-07-08, 2024.

MLS Science Team: MLS RCO2 Planned Duty Cycle Schedule, Jet Propulsion Laboratory, Aura MLS data web page, https://mls.jpl.nasa.gov/cal/r2-duty-cycle-schedule.pdf, accessed 2026-11-05, 2026.

NASA: Microwave Limb Sounder (MLS), NASA instrument web page, https://science.nasa.gov/mission/aura/mls/, accessed 2026-04-17, 2025.

NASA: Microwave Limb Sounder (MLS): Version 6 Data Release, NASA instrument web page, https://mls.jpl.nasa.gov/, accessed 2026-08-07, 2026a.

NASA: Potential Evolution of the Aura Mission, NASA Science mission web page, https://science.nasa.gov/missions/potential-evolution-of-the-aura-mission/, accessed 2026-11-05, 2026b.

NASA GES DISC: MLS/Aura Level 3 Daily Binned Water Vapor (H2O) Mixing Ratio on Zonal and Similar Grids, Version 005, Dataset landing page, https://catalog.data.gov/dataset/mls-aura-level-3-daily-binned-water-vapor-h2o-mixing-ratio-on-zonal-and-similar-grids-v005, includes recommended useful vertical range and vertical resolution information, accessed 2026-04-17, 2020.

Nash, J., Oakley, T., Vömel, H., and Wei, L.: WMO Intercomparison of High Quality Radiosonde Systems (WMO/TD-No. 1580), IOM-107, World Meteorological Organization, https://library.wmo.int/idurl/4/50499, accessed: 2026-05-22, 2011.

Navas-Guzmán, F., Martucci, G., Coen, M. C., Granados-Muñoz, M. J., Hervo, M., Sicard, M., and Haefele, A.: Characterization of aerosol hygroscopicity using Raman lidar measurements at the EARLINET station of Payerne, Atmos. Chem. Phys., 19, 11 651–11 668, https://doi.org/10.5194/acp-19-11651-2019, 2019.

Nedoluha, G. E., Bevilacqua, R. M., Gomez, R. M., Thacker, D. L., Waltman, W. B., and Pauls, T. A.: Ground-based measurements of water vapor in the middle atmosphere, Journal of Geophysical Research: Atmospheres, 100, 2927–2939, https://doi.org/10.1029/94JD02952, 1995.

NOAA Global Monitoring Division: Stratospheric Water Vapor Measurements, https://gml.noaa.gov/ozwv/wvap/sw.html, accessed: 2026-05-22, 2026.

https://doi.org/10.5194/egusphere-2026-7088
Preprint. Discussion started: 23 November 2026
© Author(s) 2026. CC BY 4.0 License.

Poltera, Y., Luo, B., and Peter, T.: Chilled mirror hygrometers and their „Golden Points“ – A new interpretation and correction method for chilled mirror data, in: Report of the Thirteenth GCOS Reference Upper Air Network Implementation Coordination Meeting (GRUAN ICM-13), online, 15 to 19 November 2021, GCOS-242 report, https://library.wmo.int/idurl/4/41928, accessed: 2026-05-22, 2021.

Poltera, Y., Luo, B., Wienhold, F. G., and Peter, T.: The “Golden Points” and nonequilibrium correction of high-accuracy frost point hygrometers, Atmospheric Measurement Techniques, 19, 5091–5134, https://doi.org/10.5194/amt-19-5091-2026, 2026.

Rolf, C., Khordakova, D., and Vömel, H.: Cfh cooling agent alternatives, in: 12th GRUAN Implementation and Coordination Meeting, Virtual, 16 to 20 November 2020, pp. 1–14, https://www.gruan.org/gruan/editor/documents/meetings/icm-12/pres/pres_302_Rolf_CFH_Cooling-Agent-Tests.pdf, accessed: 2026-05-22, 2020.

Romanens, G., Martucci, G., Rosoldi, M., Poltera, Y., Cardós, C., Prats, N., Ambe, S., Cosimato, G., Farah, A., Félix, C., Gandolfi, I., Haefele, A., Hernández, M., Iwabuchi, M., Jann, P., Lam, J. M. C., Marra, F., Rodríguez, J. M., Roulet, Y.-A., Tanaka, Y., Dirksen, R., and Madonna, F.: Assessment of humidity ground checks for GRUAN-compliant automatic radiosonde operations, EGUsphere, 2026, 1–29, https://doi.org/10.5194/egusphere-2026-3215, 2026.

Salawitch, R. J., Smith, J. B., Selkirk, H., Wargan, K., Chipperfield, M. P., Hossaini, R., Levelt, P. F., Livesey, N. J., McBride, L. A., Millán, L. F., Moyer, E., Santee, M. L., Schoeberl, M. R., Solomon, S., Stone, K., and Worden, H. M.: The Imminent Data Desert: The Future of Stratospheric Monitoring in a Rapidly Changing World, Bulletin of the American Meteorological Society, 106, E540–E563, https://doi.org/10.1175/BAMS-D-23-0281.1, 2025.

Schranz, F., Tschanz, B., Rüfenacht, R., Hocke, K., Palm, M., and Kämpfer, N.: Investigation of Arctic middle-atmospheric dynamics using 3 years of H2O and O3 measurements from microwave radiometers at Ny-Ålesund, Atmospheric Chemistry and Physics, 19, 9927–9947, https://doi.org/10.5194/acp-19-9927-2019, 2019.

Seidel, D. J., Berger, F. H., Diamond, H. J., Dykema, J., Goodrich, D., Immler, F., Murray, W., Peterson, T., Sisterson, D., Sommer, M., Thorne, P., Vömel, H., and Wang, J.: Reference Upper-Air Observations for Climate: Rationale, Progress, and Plans, Bulletin of the American Meteorological Society, 90, 361–369, https://doi.org/10.1175/2008BAMS2540.1, 2009.

Sica, R. J. and Haefele, A.: Retrieval of temperature from a multiple-channel Rayleigh-scatter lidar using an optimal estimation method, Appl. Opt., 54, 1872–1889, https://doi.org/10.1364/AO.54.001872, 2015.

SondeHub: CUSF / SondeHub Predictor, Cambridge University Space Flight and SondeHub, https://predict.sondehub.org/, accessed: 2026-05-22, 2026.

Sprenger, M. and Wernli, H.: The LAGRANTO Lagrangian analysis tool – version 2.0, Geoscientific Model Development, 8, 2569–2586, https://doi.org/10.5194/gmd-8-2569-2015, 2015.

Steiner, M., Luo, B., Peter, T., Pitts, M. C., and Stenke, A.: Evaluation of polar stratospheric clouds in the global chemistry–climate model SOCOLv3.1 by comparison with CALIPSO spaceborne lidar measurements, Geoscientific Model Development, 14, 935–959, https://doi.org/10.5194/gmd-14-935-2021, 2021.

Sun, B., Calbet, X., Reale, A., Schroeder, S., Bali, M., Smith, R., and Pettey, M.: Accuracy of Vaisala RS41 and RS92 Upper Tropospheric Humidity Compared to Satellite Hyperspectral Infrared Measurements, Remote Sensing, 13, 173, https://doi.org/10.3390/rs13020173, 2021.

Ulaby, F. T., Long, D. G., Blackwell, W. J., Elachi, C., Fung, A. K., Ruf, C. S., Sarabandi, K., Zebker, H. A., and van Zyl, J. J.: Microwave Radar and Radiometric Remote Sensing, Artech House, https://doi.org/10.3998/0472119356, ISBN 978-0472119356, 2013.

https://doi.org/10.5194/egusphere-2026-7088
Preprint. Discussion started: 23 November 2026
© Author(s) 2026. CC BY 4.0 License.

UNEP: Montreal Protocol – Kigali Amendment, chap. XXVII, 2. F Amendment to the Montreal Protocol on Substances that Deplete the Ozone Layer, https://treaties.un.org/doc/Treaties/2016/10/20161015%2003-23%20PM/Ch_XXVII-2.f-English%20and%20French.pdf, accessed: 2026-03-23, 2016.

Vaisala: Sounding System MW41 (Datasheet Ref. B211221EN-K), 2021.

Vaisala: Radiosonde RS41-SG (Datasheet Ref. B211321EN-L), 2024.

Vömel, H., David, D. E., and Smith, K.: Accuracy of Tropospheric and Stratospheric Water Vapor Measurements by the Cryogenic Frost Point Hygrometer: Instrumental Details and Observations, Journal of Geophysical Research: Atmospheres, 112, D08 305, https://doi.org/10.1029/2006JD007224, 2007.

Vömel, H., Naebert, T., Dirksen, R., and Sommer, M.: An update on the uncertainties of water vapor measurements using cryogenic frost point hygrometers, Atmospheric Measurement Techniques, 9, 3755–3768, https://doi.org/10.5194/amt-9-3755-2016, 2016.

Waters, J. W., Froidevaux, L., Harwood, R. S., Jarnot, R. F., Pickett, H. M., Read, W. G., Siegel, P. H., Cofield, R. E., Filipiak, M. J., Flower, D. A., Holden, J. R., Lau, G. K., Livesey, N. J., Manney, G. L., Pumphrey, H. C., Santee, M. L., Wu, D. L., Cuddy, D. T., Lay, R. R., Loo, M. S., Perun, V. S., Schwartz, M. J., Stek, P. C., Thurstans, R. P., and Boyles, M. A.: The Earth Observing System Microwave Limb Sounder (EOS MLS) on the Aura Satellite, IEEE Transactions on Geoscience and Remote Sensing, 44, 1075–1092, https://doi.org/10.1109/TGRS.2006.873771, 2006.

Wienhold, F. G., Germann, N., Poltera, Y., Peter, T., Körner, S., Oelsner, P., and Dirksen, R.: Peltier Cooled Frost Point Hygrometer (PCFH), Presentation at GRUAN ICM-14, Reunion Island, France, 28 November 2022 (GCOS-250 report), https://www.gruan.org/gruan/editor/documents/meetings/icm-14/pres/pres_0301e_PCFH_Wienhold.pdf, accessed 2026-04-16, 2022.

Wienhold, F. G., Poltera, Y., Peter, T., Brossi, S., and Brossi, T.: Peltier Cooled Frost Point Hygrometer (PCFH), Presentation at GRUAN ICM-15, Berne, Switzerland, 12 March 2024 (GCOS-262 report), https://www.gruan.org/gruan/editor/documents/meetings/icm-15/pres/pres_0605_Brossi_PCFH.pdf, accessed 2026-04-16, 2024.

Wienhold, F. G., Poltera, Y., Artho, V., Peter, T., Brossi, S., and Brossi, T.: Peltier Cooled Frost Point Hygrometer (PCFH), Presentation at GRUAN ICM-16, Tenerife, Spain, 20 November 2025, https://www.gruan.org/gruan/editor/documents/meetings/icm-16/pres/pres_0809_Wienhold_PCFH.pdf, accessed 2026-04-16, 2025.

WMO: Guide to Instruments and Methods of Observation (WMO-No. 8), Volume I, World Meteorological Organization, Geneva, https://doi.org/10.59327/WMO/CIMO/1, 2024:Annex 12.A.

World Meteorological Organization (WMO), Intergovernmental Oceanographic Commission of the United Nations Educational, Scientific and Cultural Organization (IOC-UNESCO), International Science Council (ISC), United Nations Environment Programme (UNEP), and Copernicus Climate Change Service (C3S): The 2022 GCOS ECVs Requirements, https://library.wmo.int/records/item/58111-the-2022-gcos-ecvs-requirements, GCOS-245, 2022 edition updated in 2025, 2025.

Wright, C. J., Hindley, N. P., Alexander, M. J., Barlow, M., Hoffmann, L., Mitchell, C. N., Prata, F., Bouillon, M.and Carstens, J., Clerbaux, C., Osprey, S. M., Powell, N., Randall, C. E., and Yue, J.: Surface-to-space atmospheric waves from Hunga Tonga-Hunga Ha'apai eruption, Nature, 609, 741–746, https://doi.org/10.1038/s41586-022-05012-5, 2022.